Sensitivity of abyssal water masses to overflow parameterizations

Kate Snow[a,*], Andrew McC. Hogg[a], Stephanie M. Downes[a], Bernadette M. Sloyan[b], Michael L. Bates[c], Stephen M. Griffies[d]

[a] *Research School of Earth Sciences and ARC Centre of Excellence for Climate System Science, The Australian National University, Canberra, Australia*
[b] *Ocean and Atmosphere Flagship, CSIRO, Hobart, Tasmania Australia*
[c] *Griffith School of Environment, Griffith University, Nathan, Queensland, Australia*
[d] *NOAA/Geophysical Fluid Dynamics Laboratory, 201 Forrestal Road, Princeton, NJ 08542, USA*

Abstract

Antarctic Bottom Water (AABW) and North Atlantic Deep Water (NADW) control the abyssal limb of the global overturning circulation and play a major role in oceanic heat uptake and carbon storage. However, current general circulation models are unable to resolve the observed AABW and NADW formation and transport processes. One key process, that of overflows, motivates the application of overflow parameterizations. A sensitivity study of both AABW and NADW properties to three current parameterizations is presented using an ocean-sea ice model within a realistic-topography sector of the Atlantic Ocean.

Overflow parameterizations that affect only tracer equations are compared to a fully dynamical Lagrangian point particle method. An overflow parameterization involving partial convective mixing of tracers is most efficient at transporting dense NADW water downslope. Such a parameterization leads to a maximum mean increase in density in the north of 0.027 kg m^{-3} and a decrease in age of 525 years (53%). The relative change in density and age in the south is less than 30% of that in the north for all overflow parameterizations. The reduced response in the south may result from the differing overflow characteristics of AABW compared to NADW. Alternative approaches may be necessary to improve AABW representation in global climate models.

Keywords: AABW, NADW, global climate models, sector model, overflow schemes

*Corresponding author
Email address: kate.snow@anu.edu.au (Kate Snow)

1. Introduction

Antarctic Bottom Water (AABW) and North Atlantic Deep Water (NADW) form important components of the global Meridional Overturning Circulation (MOC), large scale ocean stratification and distribution of oceanic heat, carbon and nutrients (Talley et al., 2003; Hughes and Griffiths, 2006; Johnson, 2008; Kuhlbrodt et al., 2007; Purkey and Johnson, 2010; Ríos et al., 2012). Properties of the deep and bottom waters throughout the global ocean are defined initially by the formation of dense shelf waters or, in part, through open ocean convection processes such as in the Labrador Sea (Zhang et al., 2011). Here we focus on the subsequent overflow processes of the shelf waters whereby the dense water flow from the continental shelf and descends down the continental slope. In the case of NADW, shelf waters are transported through the Faroe Bank Channel and Denmark Strait. Conversely, AABW flows off the Antarctic continental shelf from numerous source regions dispersed across the shelf (Baines and Condie, 1998). Due to limitations on computational resources, present generation General Circulation Models (GCMs) are unable to attain the high horizontal and vertical resolutions required to resolve overflow processes (Legg et al., 2009), thereby compromising characteristics of the resulting water masses.

Recently, several studies have indicated that abyssal water masses are key players in global climate change. For example, the recently observed contraction of AABW (Purkey and Johnson, 2012; Katsumata and Masuda, 2013), warming and freshening within the AABW and NADW density ranges (Hall et al., 1997; Levitus et al., 2005; Steinfeldt et al., 2007; Purkey and Johnson, 2010; Frajka-Williams et al., 2011; Purkey and Johnson, 2012; Couldrey et al., 2013; Sloyan et al., 2013; Zenk and Visbeck, 2013) and increase in total carbon and decrease in oxygen (Garcia et al., 1998; Sloyan et al., 2013) influences the global ocean circulation and property budgets. These results motivate us to improve simulations of AABW and NADW formation processes, in particular, overflows.

Representation of overflows in z-coordinate models (the most common vertical coordinate used in GCMs) is particularly difficult due to step-like topography (Beckmann and Döscher, 1997; Roberts and Wood, 1997; Winton et al., 1998; Ezer and Mellor, 2004; Legg et al., 2006).

Water that flows down a slope undergoes vertical convective mixing at each of these steps (refer to Figure 1a). This convection overly mixes and dilutes the overflowing waters before it reaches the bottom leading to deep water that is too warm and fresh (Winton et al., 1998; Downes et al., 2011) and bottom water that is overly warm and salty (Downes et al., 2011). Hence, overflow parameterizations have been developed to move the dense shelf water into the deep ocean, aiming to increase the density and decrease the age of AABW and NADW waters as well as increase the magnitude of the AABW and NADW overturning cells. The performance of these parameterizations in current GCMs, however, poorly represents the overflows and deep water properties, particularly in the Southern Ocean (Condie, 1995; Griffies et al., 2000; Legg et al., 2009; Downes et al., 2011; Weijer et al., 2012; Heuzé et al., 2013). Further, the limited testing of overflow parameterizations in the Southern Ocean and within models with realistic bathymetry, motivates the need to develop an increased understanding of overflow parameterizations. This paper tests the sensitivity of AABW and NADW properties and transport to three distinct overflow parameterizations, along with variations to their controlling parameters.

The overflow parameterizations tested here include the downslope transport scheme of Campin and Goosse (1999) (hereafter CG1999), the sigma bottom boundary layer scheme of Beckmann and Döscher (1997) and Döscher and Beckmann (2000) (hereafter SIGMA), and the embedded Lagrangian point-particle method of Bates et al. (2012a) and Bates et al. (2012b) (hereafter BLOBS). Note that we do not consider the overflow parameterization for the Parallel Ocean Program (POP) (Danabasoglu et al., 2010) as it was designed for NADW overflows where the flow is constrained by well defined sills or straights. Through that method, AABW source regions are confined to single regions in the Weddell and Ross Seas. We consider this approach unsuitable for the dispersed nature of AABW sources (e.g. van Sebille et al., 2013; Baines and Condie, 1998) and biases were indeed found in the representation of AABW using this method (Weijer et al., 2012); however, reasons for these biases were not provided.

We perform the sensitivity analysis within a realistic bathymetry sector of the Atlantic ocean that incorporates both the NADW source regions and the Weddell Sea, which is an

important source region for AABW (Deacon, 1937; Orsi et al., 1999; Naveira Garabato et al., 2002). Previous sector models of the Atlantic (e.g., Ezer and Mellor, 1994) do not include the South Atlantic. While the sector model described here is not a fully realistic representation of the Atlantic, it is computationally fast, allowing multiple simulations to be run whilst providing the major circulation processes commonly present in GCMs.

Our sensitivity analysis examines how the overflow schemes control AABW and NADW properties in GCMs and indicates the suitability of each parameterization to the respective overflow regions. An outline of the overflow parameterizations being tested and their defining characteristics is given in Section 2 with a review of the previous studies evaluating them. Section 3 provides the method for the set-up of the novel sector model incorporating the key processes of GCMs, followed by the defining parameter space to be tested for each scheme. Results assessing the overall performance of the sector model, a comparison of the response of AABW and NADW to each overflow scheme and the sensitivity of each scheme to parameter variations is given in Section 4. Final concluding remarks are provided in Section 5.

2. Parameterizations

2.1. Campin and Goosse (1999) (CG1999)

The CG1999 scheme is designed to move dense water downslope with minimal mixing by directly transferring tracer properties between cells. The scheme is activated when a grid cell at the bottom of a water column is adjacent to a less dense cell in a deeper water column. The tracer properties of the first cell are then transported downslope to the bottom of the adjacent water column or its neutrally buoyant level. A return flow is applied to conserve mass in a rigid lid case (refer to figure 1 of Campin and Goosse (1999)).

The downslope flux of properties is dependent on the topographic slope, S, and the density difference, $\Delta\rho$, between the shallow ocean cell and the horizontally adjacent less dense cell giving the volume flux on the slope, F, defined as

$$F = \frac{g\gamma}{\rho_0}\Delta\rho\Delta A, \tag{1}$$

where g is the gravitational acceleration, ρ_0 is a reference density taken here to be 1035 kg m^{-3}, ΔA is the cell area through which the transport is being considered and $\gamma = \frac{\delta S}{\mu}$ where δ is the fraction of the grid cell participating in the overflow and μ is the dissipation rate due to friction (Griffies, 2012). Transport may only occur between horizontally adjacent water columns.

An alternative method where no return flow is provided (Figure 1b) may be applied where the change in tracer of the deep ocean cell is defined by the downslope flux and the difference in concentration of the tracer of the shallow cell and the deep cell (Griffies, 2012) such that

$$\partial_t(V\rho C)^{do}_{kdw} = \rho F(C^{so}_{kup} - C^{do}_{kdw}), \tag{2}$$

where C is the concentration of the tracer in the shallow ocean (^{so}) and deep ocean (^{do}), $V = \Delta z\Delta y\Delta x$ is the volume of the dense water cell, kup indicates the vertical level of the shallow ocean cell and kdw the vertical level of the deep ocean cell (Figure 1a). Such a downward flux acts without the convective mixing (represented in Figure 1a) that occurs over the topographic steps. This variant of CG1999 is only possible for models with a free surface, in which there is no constant volume restriction on water columns (Bates et al., 2012a), allowing the model to adjust accordingly to the change in density and thickness of the water column (indicated in Figure 1b).

We choose the no-return flow method as the default scheme of CG1999 since this case allows for an increased exchange of dense water down the slope when analysed in an idealised slope configuration with no surface forcing (Bates et al., 2012b). However, it is advantageous to further test the return flow case as Campin and Goosse (1999) and Goosse et al. (2001) both indicate an increased downward flow of dense water for the case when a return flow is implemented.

CG1999 is recognised to have some limitations, specifically, it only identifies water columns in directly adjacent cells from the shallow water column in its search for favourable

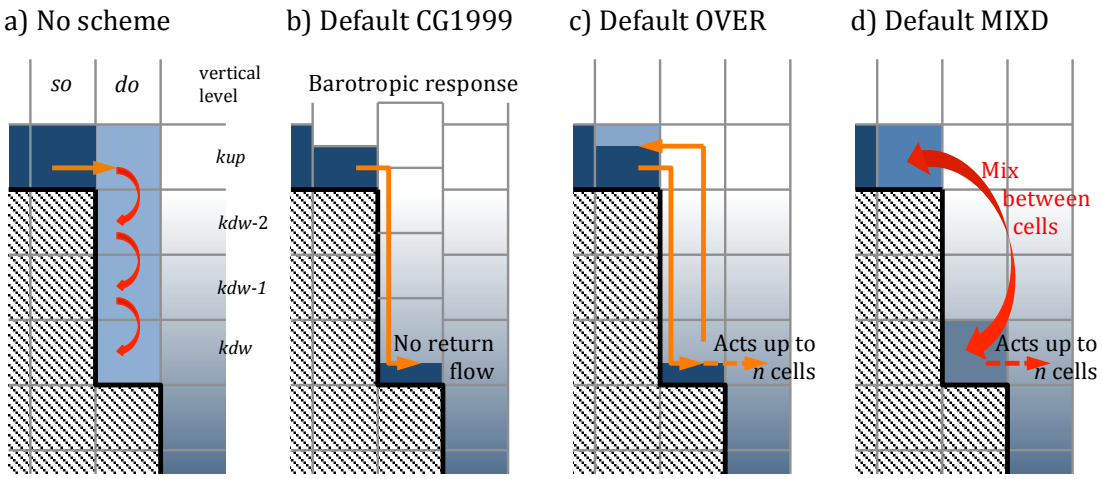

Figure 1: (a) A representation of the convection of dense water as it flows over the topographic step, (b) a representation of the no-return flow case of CG1999 where the volume flux leads to a change in water column thickness, (c) a representation of the overexchange (OVER), exchanging properties between the shallow and deep ocean grid cells and acting up to n cells and (d) a representation of mixdownslope (MIXD) where the shallow and deep cells mix towards their mean through a partial convective mixing scheme. Symbols *so* and *do* indicate the shallow and deep ocean columns respectively with the notation of the vertical levels provided in (a). The shade of blue within a cell indicates the density of water (darker = more dense).

downslope flow. Dense water travelling across regions of equal depth are therefore not affected by the scheme. Griffies (2012) recognised that such a restricted search could limit the downslope flow. Hence, the schemes of overexchange and mixdownslope (hereafter referred to as OVER and MIXD respectively) were developed to allow multiple grid cells away from the shallow dense column to be searched for favourable downslope flow.

2.1.1. Overexchange (OVER)

OVER is similar to the return flow case of CG1999 except that it allows for the exchange of tracer properties of the dense shallow water cell with the neutrally buoyant or bottom deep ocean cell without the exchange of properties of the intermediate cells (Figure 1c). Such an exchange is given by Equation (2) and (Griffies, 2012):

$$\partial_t (V\rho C)^{so}_{kup} = \rho F (C^{do}_{kdw} - C^{so}_{kup}), \tag{3}$$

The exchange of tracer properties may then occur in up to n adjacent cells (CG1999 is equivalent to $n = 1$) with the shallow cell properties being transferred along each of the n bottom cells. It is also possible to apply a weighting to the farthest cells to allow for an enhanced downslope flow. No rigorous assessment of this scheme has been previously undertaken and our results will indicate the importance of allowing for more grid cells to be included in the parameterizations when searching for favourable downslope conditions.

2.1.2. Mixdownslope (MIXD)

MIXD is similar to OVER as it allows for n grid cells to be applied in the search for downslope flows, however, in this case tracers are transferred through partial convective mixing whereby the dense shallow ocean cell partially mixes with the deep ocean cell (Griffies, 2012) (Figure 1d). MIXD does not apply a complete mixing (mixed concentration is C_{mix}) between the shallow cell concentration $C(s)$ and deep cell concentration $C(d)$, rather it applies a time tendency that mixes the concentrations towards the average (Griffies, 2012):

$$\text{tendency}(s) = \frac{M(s)\delta}{\Delta t}\left(\frac{C_{mix} - C(s)}{A}\right), \tag{4}$$

$$\text{tendency}(d) = \frac{M(d)\delta_d}{\Delta t}\left(\frac{C_{mix} - C(d)}{A}\right), \tag{5}$$

where the shallow and deep cell mass are $M(s)$ and $M(d)$ respectively, A is the horizontal area of the cells, δ is the faction of the shallow ocean cell participating in the downslope transport (and a key defining parameter to vary within the scheme) and δ_d is determined as a function of S and $\Delta\rho$. As with OVER, MIXD also allows for weighting of the farthest n cells. Although not rigorously tested in the literature, this scheme is used in the GFDL ESM2M earth system model documented by Dunne et al. (2012) as well as the Australian Community Climate and Earth System Simulator (ACCESS) (Bi et al., 2013; Marsland et al., 2013). Additionally, impacts from MIXD were seen to be non-trivial in the North Atlantic in an analysis by Palter et al. (2014) of the buoyancy budget in GFDL ESM2M under control and idealised climate change situations.

2.2. Sigma Boundary Layer (SIGMA)

The parameterization of Beckmann and Döscher (1997) and Döscher and Beckmann (2000) applies a sigma coordinate layer in the bottom cells of a z-coordinate model. The sigma layer is not affected by the convective mixing of the stepped topography and allows for diffusion and advection to occur in this layer in addition to the diffusion and advection within the z-coordinate (Figure 2).

The diffusive flux between two adjacent cells of the SIGMA scheme is given by Beckmann and Döscher (1997)

$$F_\sigma = -A \nabla_\sigma T, \tag{6}$$

where

$$A = \begin{cases} A_{max} & \text{if } \nabla_\sigma \rho \cdot \nabla H < 0 \\ A_{min} & \text{if } \nabla_\sigma \rho \cdot \nabla H \geq 0, \end{cases} \tag{7}$$

∇_σ is the horizontal gradient operator between sigma layer cells, A is the diffusivity and is maximum (A_{max}) for cases when downslope flow is favourable and minimum otherwise (A_{min}), H is the bottom depth, and T the tracer being considered.

The advective term is not assessed in this analysis as Döscher and Beckmann (2000) found it to have little impact in 1.5° horizontal resolution models. Instead, the advection term is partly accounted for via velocity dependent diffusion A_u (Griffies, 2012):

$$A_u = \begin{cases} |u| \delta x & \text{if } \nabla \rho \cdot \nabla H < 0 \text{ and } u \cdot \nabla H > 0 \\ A_{min} & \text{otherwise,} \end{cases} \tag{8}$$

where $|u|$ is the resolved sigma layer zonal velocity (we have only shown the zonal component for simplicity).

SIGMA has previously been found to produce an improved spreading of dense waters down an idealised linear slope (Beckmann and Döscher, 1997) and increased transport of dense water within a realistic bathymetry model of the North Atlantic at 1.5° horizontal resolution (Döscher and Beckmann, 2000). Bates et al. (2012b) similarly reports that the

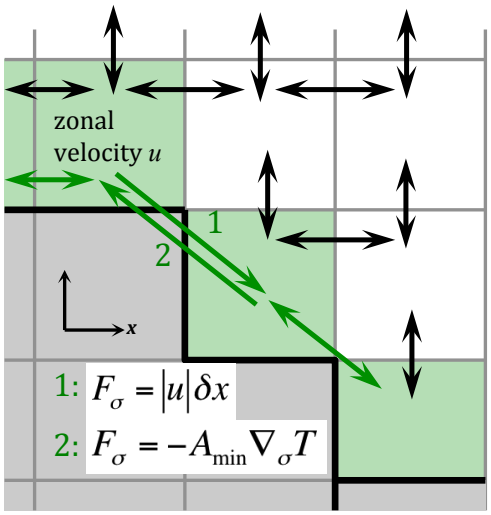

Figure 2: A representation of the velocity dependant SIGMA scheme (Equation 8) based on Griffies (2012) where the bottom sigma layer is represented by the green boxes and diffusion occurs between these grid cells (green arrows) in addition to the diffusion of the z-coordinate (black arrows).

SIGMA scheme is able to improve both the depth of penetration and slope velocities of a down flowing plume but the lack of rotational effects can also lead to a weakening of the circulation. No previous studies have tested the schemes performance in a Southern Ocean configuration.

2.3. Lagrangian point particles (BLOBS)

We test the new BLOBS parameterization developed by Bates et al. (2012a) (Figure 3). This scheme implements a system of Lagrangian point particles that interact with the Eulerian model, exchanging mass and momentum. The Lagrangian point particles may be defined as either passive or dynamic. Passive particles are created by taking a portion of the properties of the Eulerian model, transporting it downslope and returning the properties to the Eulerian model without further interaction. This case is not considered in our sensitivity analysis, as Bates et al. (2012a) found that the difference between the passive overflow scheme and the original Campin and Goosse (1999) scheme is of the order of machine error. Further, free Lagrangian particles (that is particles that move freely through the open ocean away from bottom boundaries) will not be included due to their non-hydrostatic nature potentially

leading to large vertical velocities and instabilities. In this study, only bottom grid cell Lagrangian particles are considered as these are the particles that affect the formation rate and properties of AABW and NADW.

Bottom particles are created when the difference in density between the dense shallow and less dense deep ocean cell is greater than the defined threshold $\Delta\rho$. The Lagrangian particles then transport mass and momentum, while interacting with the bottom grid cells of the Eulerian model, until they are destroyed and their properties returned to the Eulerian model (Figure 3).

The simplicity of the point particles definition allows a more complete set of dynamics, and hence a more complete representation of overflow processes, to be applied to the Lagrangian framework (Bates et al., 2012a). For example, BLOBS includes non-hydrostatic momentum and an entrainment parameterizations based on Price and Baringer (1994). In idealised model set-ups (the DOME by Legg et al. (2006) and bowl by Winton et al. (1998)), the dynamic bottom BLOBS scheme enhances downslope transport and circulation response due to more realistic dynamics than previous overflow schemes (Bates et al., 2012b). Note however, a recently discovered coding error reduces the increase in circulation of the bowl case given in Bates et al. (2012b) (Appendix A). The computational overhead of BLOBS is proportional to the number of active Lagrangian particles, with the bowl test case leading to a 16-117% increase in computational time and insignificant increase in the DOME case (Bates, 2011). However, BLOBS is yet to be tested outside an idealized model configuration.

3. Model and Methods

We define a model domain that allows a range of sensitivity tests to be performed for each of the overflow parameterizations. A computationally fast domain is required due to the large number of model runs that need to be performed. We also need a model that represents all the key characteristics of current GCMs and the factors that affect AABW and NADW formation. Hence, a 1° horizontal resolution sector model of the Atlantic, the primary formation regions of AABW and NADW, is developed.

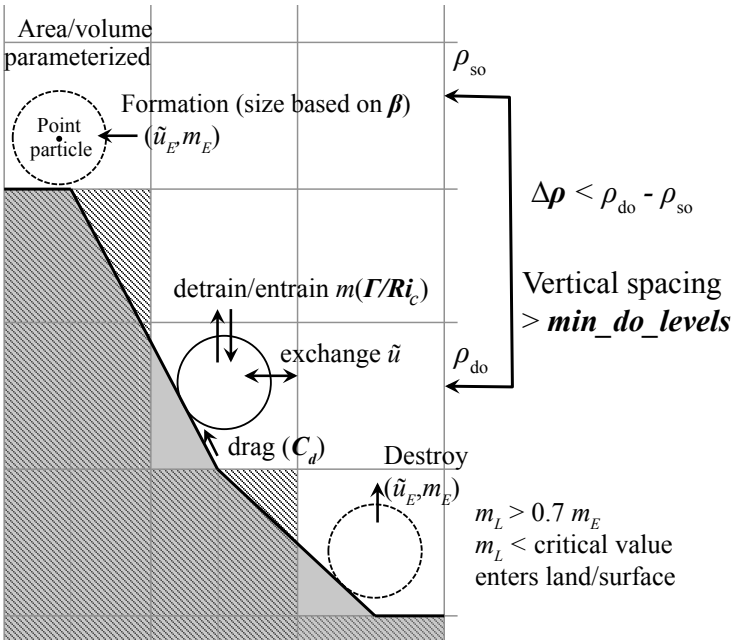

Figure 3: A representation of the dynamic bottom BLOBS scheme (based on Bates et al. (2012a)). Dashed circles indicate Lagrangian particle formation and destruction while a solid circle is an active particle with mass and momentum in the Lagrangian system given by m_L and $\tilde{u}_L$ and in the Eulerian system by m_E and $\tilde{u}_E$. Methods for particle destruction are given in the bottom right with conditions for formation above. Hatched grid cells are land points while shaded regions indicate the effective bathymetry seen by the Lagrangian particles (Bates et al., 2012a). Parameters here are; bottom drag (C_d), the detrainment parameter (Γ), the critical Richardson number (Ri_c), $\beta = \frac{\delta}{\mu}$, and the minimum vertical spacing to allow Lagrangian particle formation (min_do_levels). Each parameter is defined in more detail in Section 3.3.3

3.1. Sector Domain

The Atlantic sector is created by scaling topography derived from the NOAA/GFDL 1/4° model global bathymetry (Delworth et al., 2012) and the Weddell Sea coast of the ETOPO2 version 2 globally gridded 2 minute ocean and land topography, referred herein as ETOPO2 (U.S. Department of Commerce, National Oceanic and Atmospheric Administration, National Geophysical Data Center, 2001).The ETOPO2 data is only used where the GFDL bathymetry has idealised straight edge boundaries along the Weddell Sea coast; at all other locations we choose the GFDL bathymetry due to its proven applicability within the model's framework. The ETOPO2 data replaces the GFDL bathymetry between the

sector latitudes of 78.47°S to 70.74°S and longitudes of 3.375°E to 30.123°E (corresponding to global longitudes of 72°W to 35°W) and smoothing is applied at the ETOPO2 and GFDL boundary to ensure no sharp edges are created.

Two piecewise-linear boundaries set the longitudinal limits of the domain (red lines in Figure 4a). The topography within the boundary region is deformed at each latitude via a linear mapping to a fixed 60° wide section and interpolated to a 1/4° Mercator grid (Figure 4b). The boundaries are chosen to follow land masses and so create closed wall boundaries everywhere except Drake Passage. Periodic boundary conditions are applied at Drake Passage to simulate the Antarctic Circumpolar Current (ACC); the land boundary is defined so that the two Antarctic eastern and western edges, and the Africa-South America boundary match (Figure 4c). Due to this 60° wide boundary restriction and the increased computational efficiency of a reduced domain, our configuration is advantageous over an approach that does not deform the bathymetry and uses a land fill to remove the ocean outside the boundary region. Also, land filling does not permit a smooth transition of the topography for the periodic ACC flow and requires more land points to be taken into account in the model computations.

Following the deformation and smoothing, all inland lakes and the Mediterranean Sea are filled in, land is added to the eastern and western boundaries to ensure no re-entrant regions outside Drake Passage and some minor smoothing of the Antarctic and North Atlantic continental slopes is performed (Figure 4b). With the model set-up initially at $\frac{1}{4}^\circ$ resolution, the topography is then interpolated to create the 1° resolution domain used in this study. 1° is chosen over $\frac{1}{4}^\circ$ due to the need for computational speed; higher resolution simulations are ongoing.

While the deformation may influence the shape of important regions of deep and bottom water pathways (e.g. the mid-Atlantic ridge), the bathymetry retains the primary features that control both AABW and NADW flow. Despite the shift of the mid-Atlantic ridge, the AABW (and NADW) follows the expected path, moving along the western continental rise south (north) of the equator and flowing against the mid-Atlantic ridge north (south) of the equator.

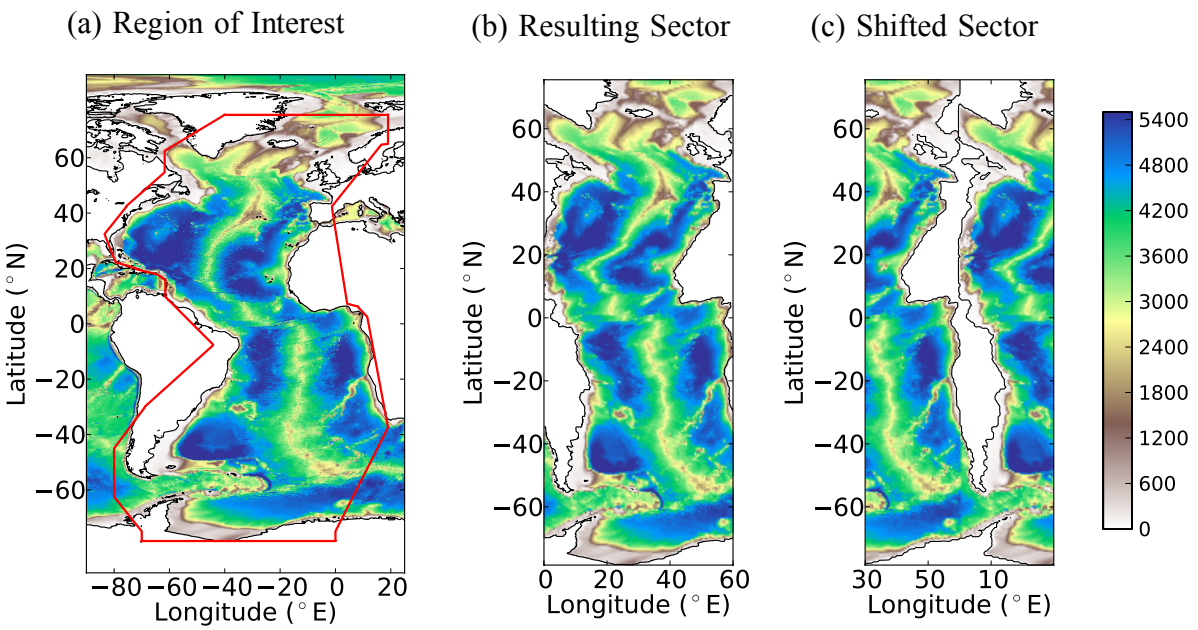

Figure 4: (a) The defined boundaries for the domain of the sector, with the GFDL bathymetry shown only in this case. The region within the boundary is deformed to fit a 60° wide sector resulting in (b) with smoothing across the boundary for the periodic ACC indicated by the smooth transition in the shifted sector in (c).

3.2. Model Properties

The Modular Ocean Model version 5 (MOM5, Griffies (2012)) is chosen to represent the ocean. The model employs a z^* vertical co-ordinate with partial cells and gradually increasing vertical grid spacing from 10 m at the surface to 200 m at depth, providing a total of 65 vertical levels to 5.5 km deep. Horizontal resolution of 1° is used employing the Gent and McWilliams (1990) eddy parameterization and the Fox-Kemper et al. (2008) parameterization of submesoscale eddies. The KPP surface boundary layer scheme of Large et al. (1994) is used, along with the interior gravity wave induced mixing scheme of Simmons et al. (2004) and the coastal tide mixing scheme of Lee et al. (2006). The background diffusivity is defined as 1×10^{-5} m^2 s^{-1} and the background viscosity as 5×10^{-5} m^2 s^{-1}. Horizontal frictional dissipation is achieved through the biharmonic Smagorinsky viscosity scheme (Griffies and Hallberg, 2000), however a Laplacian operator is employed in the lower five points of the model to maintain the stability of the model on small partial cells near

the shelves.

The nonlinear equation of state of Jackett et al. (2006) is applied, as the physical processes involved in the overflows include nonlinear effects such as cabbelling and thermobaricity (McDougall, 1987; Gordon et al., 1993; Foldvik et al., 2004; Urakawa and Hasumi, 2012). The ocean model is coupled to the GFDL Sea Ice Simulator (SIS) (Winton, 2000), which is run on the same Mercator grid as the ocean model. A non-linear equation for the frazil ice formation is applied as we find that the linear form significantly decreases (by order 0.05 kg m^{-3}) the shelf water densities on the Antarctic shelf (Appendix B), an undesirable effect as it decreases the flow of water down the slope. The Coordinated Ocean-ice Reference Experiments (CORE) Normal Year Forcing (Large and Yeager, 2009) atmospheric state is coupled to the ocean and ice model. The CORE product is deformed in the same manner as the bathymetry after first being interpolated to a $\frac{1}{4}^{\circ}$ resolution for the deformation process, and then to 1°. Applying the same deformation procedure allows for continuity between the devised ocean and land and the atmosphere.

The model is initiated from the January Levitus (1994) climatology in the World Ocean Atlas (WOA 2009) with the temperature and salinity fields deformed in the same manner as the global bathymetry. Sea surface salinity is restored to monthly climatologies that have similarly been deformed. The model is then spun-up for 2660 years to a control state where sufficient AABW and NADW is produced to allow a suitable sensitivity analysis of the overflow parameterizations.

3.3. Parameter Space

The control run (CTR), excludes any overflow scheme and reaches equilibrium (defined by <10% change in zonal mean age per 200 years, averaged over the entire domain) at 2660 years. Each of the separate overflow schemes are applied individually starting from year 2660 and run for 200 years. The parameters chosen for each run (defined below) are varied about recommended default values to explore a suitably large parameter space that encompasses the range of responses possible from the schemes.

3.3.1. CG1999, MIXD and OVER

A summary of the parameter choices for testing CG1999, MIXD and OVER is given in Table 1. The key tuneable parameter of CG1999 is $\gamma = \frac{\delta S}{\mu}$ (Equation (1)); however, since slope S is not an external parameter, we define $\beta = \frac{\delta}{\mu}$ as the primary parameter to be varied in the sensitivity analysis.

Campin and Goosse (1999) recommend values of $\delta = \frac{1}{3}$ and $\mu = 10^{-4}$ s^{-1}, hence $\beta_0 = \frac{1}{3} \times 10^4$ s is used as the default value. To obtain a suitable spectrum of parameters, δ is varied within the bounds of the parameter (δ =0.1 and 2/3) and μ is varied by an order of magnitude in either direction ($\mu = 10^{-3}$ s^{-1}, 10^{-5} s^{-1}). These parameters give β values of $0.3\beta_0$, $2\beta_0$, $0.1\beta_0$ and $10\beta_0$ respectively. Both return flow and no return flow cases are considered.

OVER has the same defining β parameter as CG1999, but now with the additional parameter determining the number of grid cells (n) used in the search for the neutral buoyancy level. Due to the similarity between OVER and CG1999, fewer values of β are tested.

In MIXD, the defining parameters vary from CG1999 and OVER due to the partial mixing of tracers of this method. The defining parameters of MIXD are δ_s (the fraction of the shallow ocean cell participating in the downslope flow) and n. Again, due to similarity of this scheme to both CG1999 and OVER, only limited parameter choices are considered. Applying a weighting term (*weight*) for farther cells is also considered for OVER and MIXD where an increased fraction of tracer is transported to furthest n cells, rather than an equivalent fraction across each of the n cells. For the MIXD case, a final option where the scheme is set at the default parameters but a mask is applied removing the scheme from the northern half of the sector is tested. This run, referred to as *mask*, allows us to attribute changes to northern or southern overflow processes.

3.3.2. SIGMA

The SIGMA parameter variations are given in Table 2. The default case is chosen as the case where a velocity dependent diffusion is applied (Equation 8). The defining parameter for such a case is the sigma diffusivity ratio $\kappa_\sigma^{ratio} = A_{min}/A_{max}$ (or $\kappa_\sigma^{ratio} = A_{min}/|u|\delta x$ for

Run	β (s) or δ_s	return flow(CG1999) or weighted(MIX,OVER)	n
CG1999 (default)	$\boldsymbol{\beta = \beta_0}$	**false**	**1**
CG1999 ($0.1\beta_0$)	$\beta = 0.1\beta_0$	false	1
CG1999 ($0.3\beta_0$)	$\beta = 0.3\beta_0$	false	1
CG1999 ($2\beta_0$)	$\beta = 2\beta_0$	false	1
CG1999 ($10\beta_0$)	$\beta = 10\beta_0$	false	1
CG1999 (rf)	$\beta = \beta_0$	true	1
OVER (default)	$\boldsymbol{\beta = \beta_0}$	**false**	**1**
OVER ($0.3\beta_0$)	$\beta = 0.3\beta_0$	false	1
OVER ($10\beta_0$)	$\beta = 10\beta_0$	false	1
OVER ($n = 2$)	$\beta = \beta_0$	false	2
OVER ($n = 6$)	$\beta = \beta_0$	false	6
OVER ($weight$)	$\beta = \beta_0$	true	6
MIX (default)	$\boldsymbol{\delta_s = 0.333}$	**false**	**1**
MIX ($\delta_s = \frac{2}{3}$)	$\delta_s = 0.666$	false	1
MIX ($\delta_s = 1.0$)	$\delta_s = 1.0$	false	1
MIX ($n = 2$)	$\delta_s = 0.333$	false	2
MIX ($n = 4$)	$\delta_s = 0.333$	false	6
MIX ($weight$)	$\delta_s = 0.333$	true	6
MIX ($mask$ = south only)	$\delta_s = 0.333$	false	1

Table 1: Parameter domain of CG1999, MIXD and OVER for varying β, δ_s, and n, with options for weighted runs and implementing return flow. Refer to the text for further details.

Run	κ_σ (m^2 s^{-1})	κ_σ^{ratio}	velocity dependent diffusivity
SIGMA (default)	**N/A**	$\mathbf{10^{-6}}$	**true**
SIGMA ($\kappa_\sigma^{ratio} = 10^{-4}$)	N/A	10^{-4}	true
SIGMA ($\kappa_\sigma^{ratio} = 10^{-8}$)	N/A	10^{-8}	true
SIGMA ($\kappa_\sigma = const$)	10^3	10^{-6}	false

Table 2: Parameter domain of SIGMA for varying κ_σ and κ_σ^{ratio} and the option of implementing constant diffusivity. Refer to the text for further details.

the velocity dependent case) with A_{max} and A_{min} defined in Equation (7). The recommended default value of κ_σ^{ratio} (1×10^{-6}, the default within MOM5) is applied with variations by two orders of magnitude (1×10^{-4} and 1×10^{-8}). A final variation through the application of a constant diffusivity $\kappa_\sigma = A_{max}$ (Griffies, 2012) is investigated with the magnitude chosen based on the scheme's preset value of 1×10^3 m^2 s^{-1}.

3.3.3. BLOBS

The parameter variations for BLOBS are summarised in Table 3 and their application within the Lagrangian system is represented in Figure 3. Numerical parameters such as the relative error of the Runge-Kutta and time step are ignored as they do not affect the physical parameters. The parameters to be tested are β, the dimensionless bottom drag coefficient C_d, the detrainment parameter Γ and the critical Richardson number Ri_c defining the degree of entrainment.

We define the number of particles formed by setting the minimum density difference between shallow and deep ocean cells that permits the creation of a Lagrangian particle, $\Delta\rho$, to 0.013 kg m^{-3} and the minimum slope on which a Lagrangian particle is formed, min_do_levels, to 5 (see Figure 3). This choice is a pragmatic value, taking into account the computational cost of BLOBS and defining shelf densities in the CTR case. With the default values chosen, we test the influence of increased and decreased particle formation rates through increasing/decreasing $\Delta\rho$ and min_do_levels (the $more/less$ cases in Table 3)

Bates et al. (2012b) tested variations of the detrainment parameter (Γ), determining that the degree of detrainment was less sensitive to change when Γ was decreased below 5×10^{-8} kg m^{-2} s^{-1}; we perform similar tests in a realistic ocean configuration. Hence,

Run	β (s)	C_d	Γ (kg m^{-2} s^{-1})	Ri_c	min_do	$\Delta\rho$
BLOBS (default)	$\boldsymbol{\beta_{0b}}$	$\mathbf{3 \times 10^{-3}}$	$\mathbf{5 \times 10^{-8}}$	**0.8**	**5**	**0.013**
BLOBS ($4\beta_{0b}$)	$4\beta_{0b}$	3×10^{-3}	5×10^{-8}	0.8	5	0.013
BLOBS ($0.5\beta_{0b}$)	$0.5\beta_{0b}$	3×10^{-3}	5×10^{-8}	0.8	5	0.013
BLOBS ($C_d = 3 \times 10^{-2}$)	β_{0b}	3×10^{-2}	5×10^{-8}	0.8	5	0.013
BLOBS ($C_d = 3 \times 10^{-4}$)	β_{0b}	3×10^{-4}	5×10^{-8}	0.8	5	0.013
BLOBS ($Ri_c = 0.4$)	β_{0b}	3×10^{-3}	5×10^{-8}	0.4	5	0.013
BLOBS ($Ri_c = 1.2$)	β_{0b}	3×10^{-3}	5×10^{-8}	1.2	5	0.013
BLOBS ($\Gamma = 5 \times 10^{-7}$)	β_{0b}	3×10^{-3}	5×10^{-7}	0.8	5	0.013
BLOBS ($\Gamma = 5 \times 10^{-9}$)	β_{0b}	3×10^{-3}	5×10^{-9}	0.8	5	0.013
BLOBS ($more$)	β_{0b}	3×10^{-3}	5×10^{-8}	0.8	2	0.010
BLOBS ($less$)	β_{0b}	3×10^{-3}	5×10^{-8}	0.8	8	0.016

Table 3: Parameter domain of BLOBS where β, C_d, Ri_c and Γ are the varied parameters along with the number of active particles formed through min_do_levels (shortened to min_do above to conserve space) and $\Delta\rho$. For details refer to the text.

a default of 5×10^{-8} kg m^{-2} s^{-1} is chosen with variations to 5×10^{-7} kg m^{-2} s^{-1} and 5×10^{-9} kg m^{-2} s^{-1}. The critical Richardson number defining the degree of entrainment is tested about the suggested default value of 0.8 (Bates et al., 2012b), increasing and decreasing it to 1.2 and 0.4 respectively.

The parameter β is applied in BLOBS as the scheme relies on a similar processes to CG1999 in determining the initial formation of a Lagrangian particle. Hence, β is used to calculate, for example, the initial size of the particle relative to the grid cell volume. The default β for BLOBS is defined as β_{0b} and chosen to be 0.16666. Variations increasing and decreasing β to $\frac{1}{2}\beta_{0b}$ and $4\beta_{0b}$ are tested.

Bates et al. (2012b) determined that increasing the bottom drag decreases the downslope speed and increases the depth that the particles penetrates in an idealised slope configuration. We choose the default bottom drag based on that suggested by Bates et al. (2012b) ($C_d = 3 \times 10^{-3}$) and test the model's sensitivity to an order of magnitude increase and decrease about this value.

The default value of the minimum mass of the Lagrangian particles before they are destroyed (1×10^3 kg) will not be considered in the sensitivity study as smaller values can lead to roundoff errors and numerical errors (Griffies, 2012). Similarly, the default value of

the maximum portion of a grid cell that a Lagrangian particle may occupy (0.7) will be held constant, as Bates (2011) found that a larger value results in the bottom cells constraining the particle mass.

3.3.4. Model runs

The yearly temperature, salinity, density, age and transport are assessed to diagnose the effect of varying overflow schemes and parameters on the overturning and deep ocean properties. Here, age is defined as the time since the water has been in contact with the surface. Note, there is no model diagnostics for the mass transport of the Lagrangian particles, therefore their contribution is not included in calculations of the overturning streamfunction. However, the particles influence on the Eulerian model may still be partly discerned through the changes they induce compared to CTR.

Many of the results are simplified to a time mean of the last 20 years to provide an indication of the overflow scheme's overall performance. Two regions are used to diagnose the overflow scheme's impact in the northern and southern Atlantic regions; the north region is the zonally and meridionally averaged region from 32.4°-62.4°N and represents a 30° area south of the Denmark Strait, and the south region is zonally and meridionally averaged within 44.7°-74.7°S and represents the region 30° north of the Antarctic slope edge. These regions are chosen for the analysis as it allows both north and south responses to be quantified separately and hence the sensitivity of each scheme to AABW and NADW overflows. We choose the north/south regions to encompass the areas extending from the northern/southern edge of the overflows. This area is large enough that the influence the schemes have on the downstream deep and bottom water properties can be clearly assessed.

4. Results

4.1. Model Performance

Due to the novel nature of the sector model, a brief model evaluation of the control state is presented. At 2660 years, the ACC transport is approximately 50 Sv, appearing to have reached equilibrium (not shown). This transport is less than half the observed

value (137±7 Sv; Meredith et al., 2011). At $\frac{1}{4}^{\circ}$ resolution the Drake Passage transport is 84 Sv, indicating resolution affects the transport here. Further, factors influencing the ACC outside the Atlantic (e.g. $\approx$ 15 Sv transport provided by Indonesian Through-flow to ACC (Sprintall et al., 2009)) are not included in the sector model.

The decadal mean NADW transport at 30°N (defined as the maximum in the upper overturning cell in potential density space referenced to 2000 m, σ_2>36.6 kg m^{-3}) and the AABW transport at 30°S (defined as the maximum in the lower overturning cell in potential density space, σ_2>36.6 kg m^{-3}) are found to be 3.6 Sv and 2.2 Sv respectively (Figure 5). There is a strong pole-to-pole upper overturning cell, indicated by the red streamlines outcropping in the Southern Ocean. The low NADW transport and maximum cell transport of 7 Sv (compared to max Atlantic Meridional Overturning Circulation (AMOC) of e.g. 18 Sv at 26.5°N from RAPID observations; Johns et al., 2011), is likely due to the incomplete representation of factors that contribute to the NADW, such as the closed wall boundary in the north and the closed Mediterranean overflow. The latter, however, is partially accounted for with surface salinity restoring and so we expect the influence of the closed Mediterranean to be less than 1 Sv (Rahmstorf, 1998; Chan and Motoi, 2003; Ivanovic et al., 2014).

The CORE NYF surface forcing may also influence the AABW and NADW transports (Gerdes et al., 2006) along with open ocean convection processes (Zhang et al., 2011). With only the Weddell Sea source region included in the sector, a weaker AABW transport is expected as we have included only one sixth of the Antarctic coastline. Finally, the lack of an overflow scheme in CTR we would expect descending deep and bottom waters to be overly influenced by the convective mixing on the topographic steps (e.g., Beckmann and Döscher, 1997; Winton et al., 1998; Legg et al., 2006). Despite the relatively weak NADW and AABW transports, we obtain a representation of NADW- and AABW-like overflows and water masses that show similar interactions (not necessarily of the same magnitude) and properties to those expected. We argue that such transport is sufficient to provide an evaluation of the sensitivity of the overturning circulation to the overflow parameterizations.

The model density and tracer fields (Figures 5c and 6) are similar to those found in the

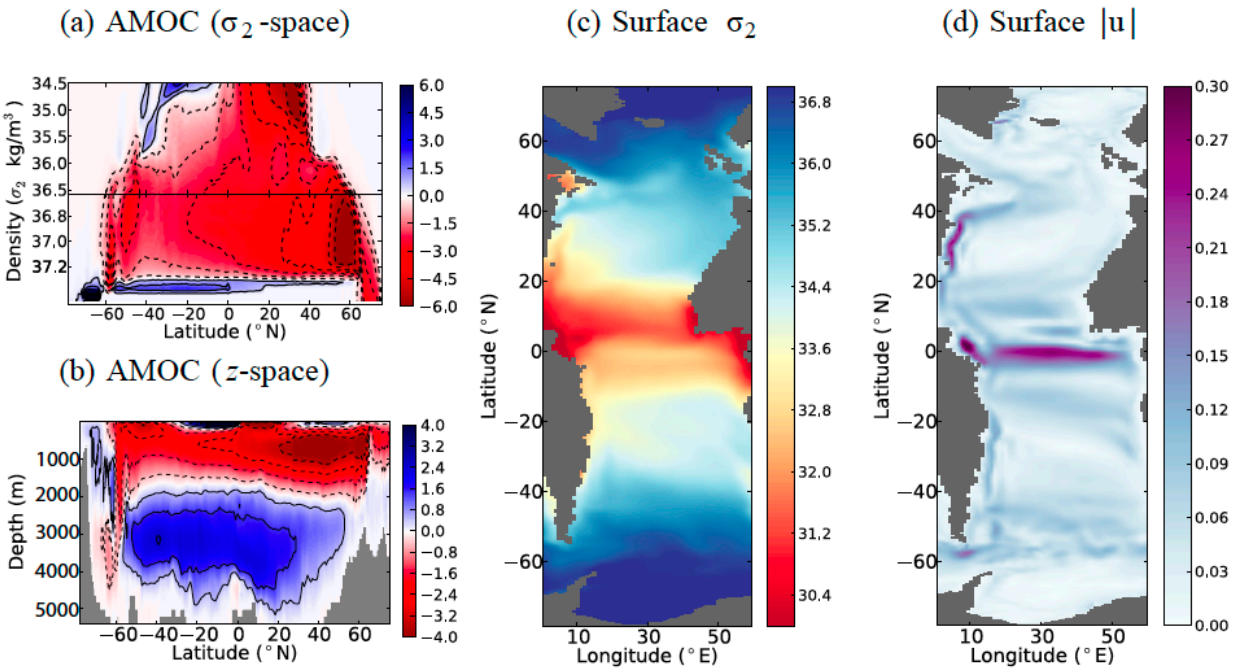

Figure 5: 10 yr mean state from 2660-2670 years for 1° resolution sector model with (a) Meridional Overturning (Sv) in density space and (b) z-space where contours are at unit intervals from 0.5 and -0.5 (with negative indicating clockwise overturning), (c) Surface density in σ_2 (kg m^{-3}) and (d) absolute mean surface velocity (m s^{-1}).

global climate model configurations using the MOM4p1 ocean component (Dunne et al., 2012; Danabasoglu et al., 2014), however there is a cool and fresh bias compared to observations. Despite the transformed sector shape, many of the major surface circulation pathways (e.g. equatorial currents and western boundary currents) are reproduced (Figure 5d). The range of processes available in this sector is a step forward compared to idealised bathymetry sectors (e.g., Hogg et al., 2013; Munday et al., 2013) where much of the dynamics and forcing are also idealised and so are unable to incorporate all the key factors of a GCM.

4.2. Parameterizations Comparison

The five different default parameterization schemes of CG1999, OVER, MIXD, SIGMA and BLOBS are initially compared to each other and to CTR in the north and south analysis regions. With only a 200 year model period, further changes are expected if the simulations continued, however computational constraints do not permit equilibration. Due to the ap-

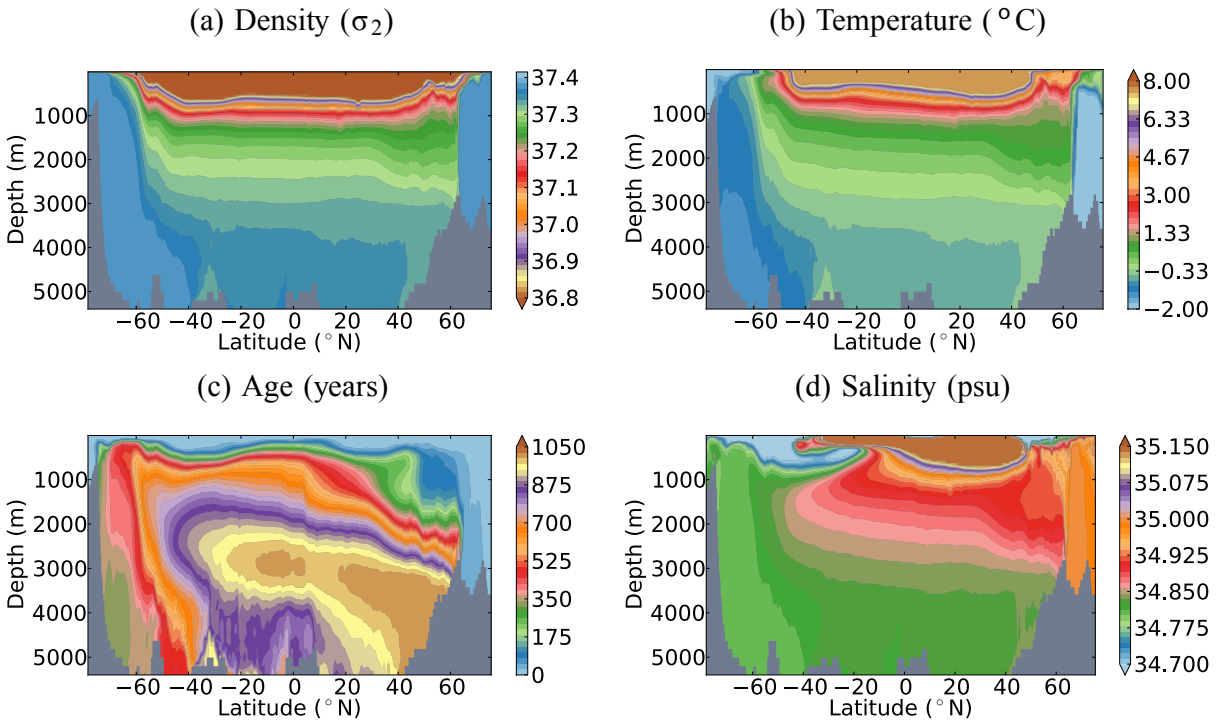

Figure 6: 10 yr mean state from 2660-2670 years for the 1° resolution sector model with zonally averaged fields of (a) potential density in σ_2 (kg m^{-3}), (b) temperature (°C), (c) age (years) and (d) salinity (psu).

proximately constant trends in the last 100 years (Figure 7), the model change compared to CTR and relative sensitivity produced by each scheme is well represented within this period. In fact, it is clear after only 50 years that MIXD dominate in the north and south, leading to an increase in density and decrease in age. Hence a time mean of the last 20 years is a suitable measurement of the sensitivity of each overflow scheme.

Profiles of area-averaged temperature, salinity, density and age differences from CTR for the years 180-200 are found for the north and south regions (Figure 8). The greatest response in both the north and south is produced by MIXD. In the north, MIXD leads to saltier and warmer waters descending below 2000 m and 2500 m respectively. With the density response dominated by salinity, the tracer changes produce a maximum increase in density below the surface of 0.02 kg m^{-3} at 2500 m and a decrease in age of 400 years (42%) at 3200 m. Note, the change in age is greater than the period of the model run (200

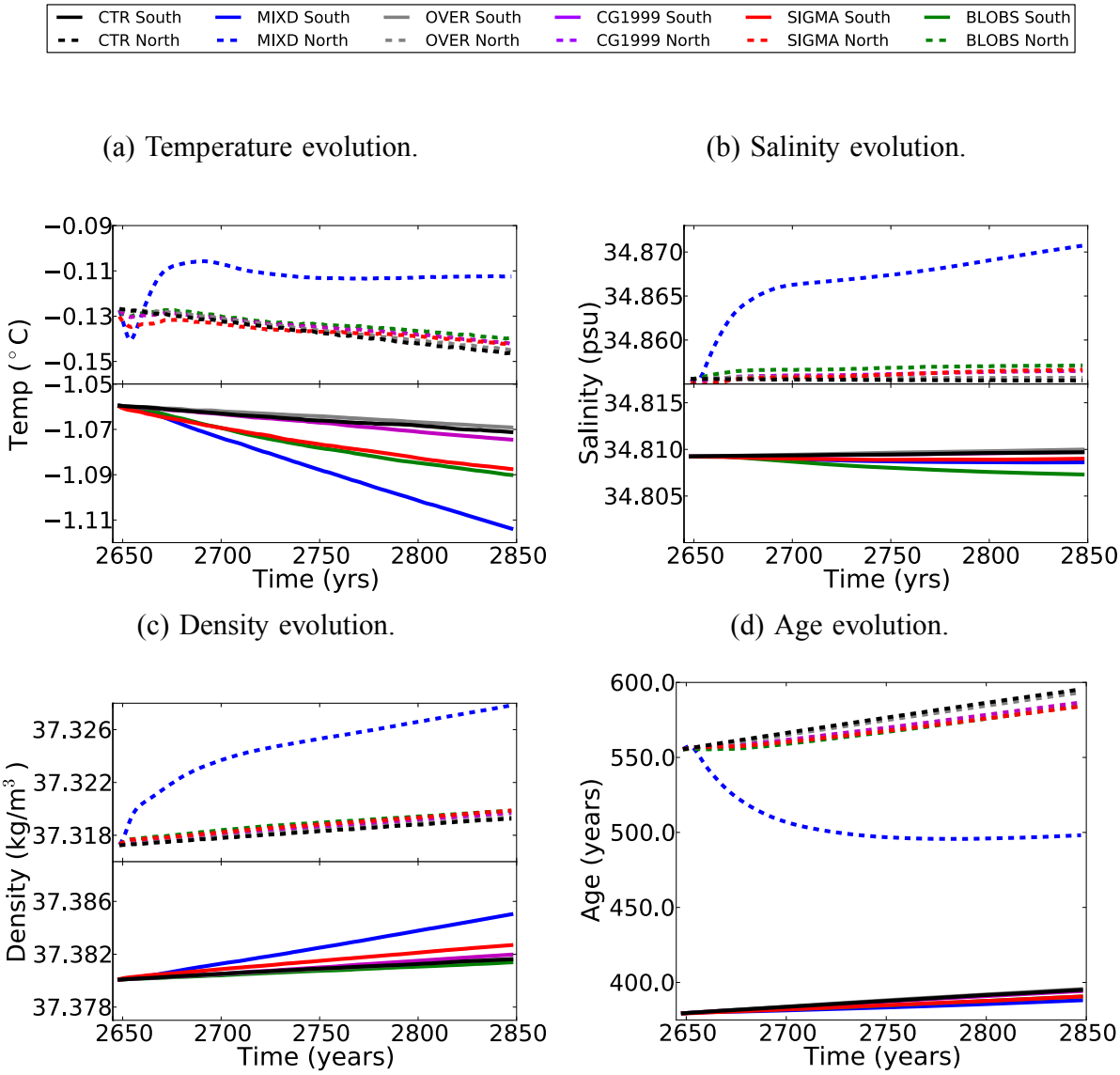

Figure 7: Evolution of (a) temperature (°C), (b) salinity (psu), (c) density in σ_2 (kg m^{-3}) and (d) age (years) for the default setup of each scheme over the 200 years the overflow schemes are applied (coloured lines) compared to CTR (black) where no overflow scheme is applied. Quantities are calculated as the average of the bottom two grid cells below 2 km in the region 30° south of the Denmark Straight (dashed lines) and the region 30° north of the Antarctic slope edge (solid lines). Note the discontinuity in the vertical axes of (a), (b) and (c), and the CG1999 is often overlaid by the CTR case.

years) due to changes in circulation that alter the regions of differently defined age water masses. In the south, the changes are much smaller. While cooler and slightly fresher waters

descend the south in MIXD leading to an increase in density and decrease in age over the water column, the magnitudes (0.003 kg m^{-3} and 20 years respectively) are just 30% the vertically integrated absolute change in density and 10% of the age changes produced in the north.

The effect of CG1999, OVER, SIGMA and BLOBS on tracer properties is negligible (<3% change in age and <0.2% in density) in the south (solid lines in Figure 8)). Measurable changes are found in the north region (dashed lines), where age decreases by a maximum of 40 years (5%) at 2750 m for these schemes and changes in temperature and salinity lead to an increase in density below the surface by a maximum of 0.005 kg m^{-3} at 1750 m.

The difference in the MOC from the CTR (Figure 9) for the last 20 years for CG1999, OVER, SIGMA or BLOBS (Figure 9a, 9b, 9c and 9d respectively) shows minimal change in the AABW anti-clockwise cell. However, OVER, SIGMA and BLOBS each increase the density of the clockwise NADW cell (the negative red band in Figure 9) without significantly altering (to an error of 1%) the maximum streamfunction and hence our diagnostic of NADW transport. BLOBS provide a larger change in circulation in the north than CG1999, supporting the updated results of Bates et al. (2012b) that take into account code error (Appendix A). We stress that the BLOBS Lagrangian particle contribution to the overturning is not included in the calculated streamfunctions producing some uncertainty in the specific values of the streamfunction. The particles exclusion from the transport term also leads to the spike observed in Figure 9d at 20°N where a large number of particles are accumulating and being destroyed, returning their momentum and mass properties to the Eulerian model. The overall influence and order of magnitude of the BLOBS scheme on the Eulerian model may still be interpreted from the streamfunctions as particle lifetimes are often less than one year and results shown are at 200 years. A similar approach for the barotropic streamfunction was applied in Bates et al. (2012b).

MIXD (Figure 9e) provides the greatest change in the north, increasing the density of the NADW cell throughout the model domain. However, the movement of water to greater densities distributes the NADW over a greater depth range, reducing the peak of the anti-clockwise cell so that the defined NADW transport decreases by 0.2 Sv (5%). MIXD also

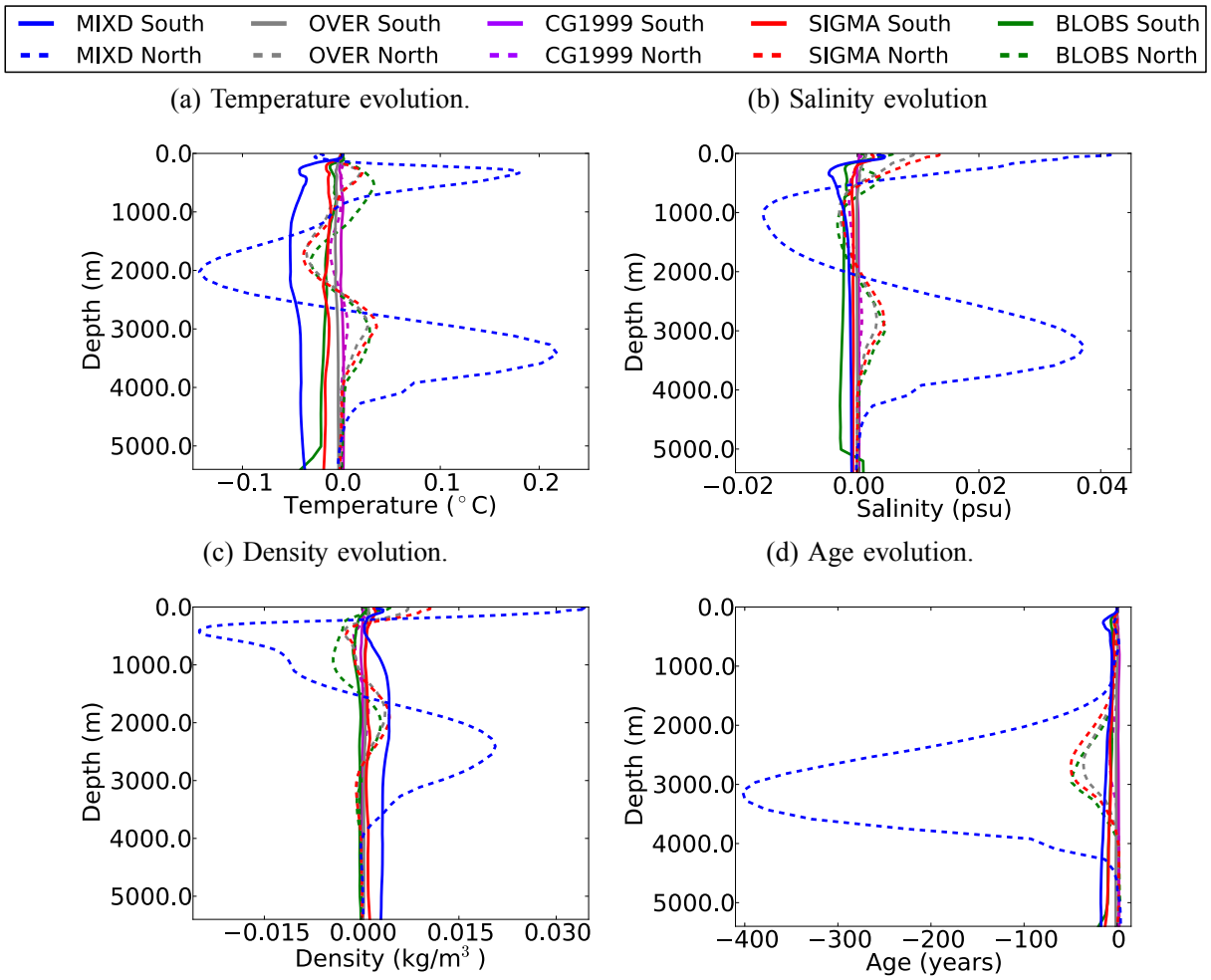

Figure 8: Mean difference from CTR in (a) temperature (°C), (b) salinity (psu), (c) density (kg m^{-3}) and (d) age (years) averaged over the region 32.4°N-62.4°N (dashed lines) and 44.7°S-74.7°S (solid lines) versus depth for each of the different parameterizations. The difference is defined as the time average of the last 20 years in the overflow scheme runs minus the equivalent of the CTR. Note, that profiles of CG1999, OVER and SIGMA overlie in the south.

441 produces a slight increase in density of the AABW cell southward of 20°N. In this case
442 the increase occurs over the region where the peak transport of the cell occurs, thereby
443 increasing AABW transport by 0.2 Sv (9%).

444 The minimal change produced by CG1999 may be expected based on the results of
445 Goosse et al. (2001). They found only a relatively weak response of AABW to the return
446 flow CG1999 case with the application of realistic surface forcing (the more complete AABW

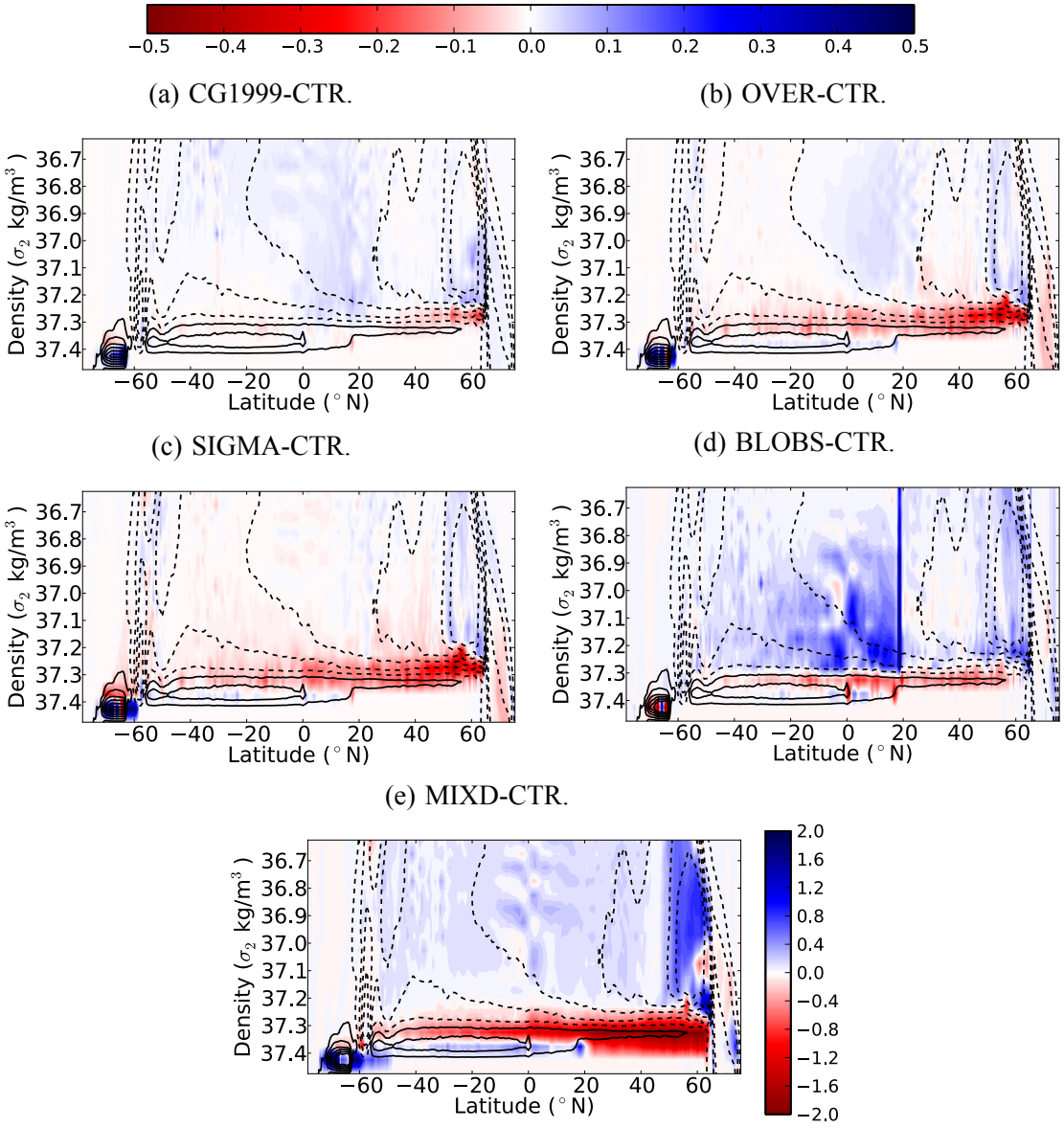

Figure 9: Difference in meridional overturning (Sv) from CTR in potential density space referenced to 2000 m (σ_2) for the cases (a) CG1999, (b) OVER, (c) SIGMA, (d) BLOBS and (e) MIXD for years 180-200 in the default parameter runs. The contours represent the mean overturning of CTR in this period with solid contours indicating anti-clockwise overturning and dashed clockwise at unit intervals starting at 0.5 and -0.5 respectively with a positive (blue) change indicating an increase in anti-clockwise flow while negative (red) is an increase in clockwise flow. Note the different colour bar for panel (e).

representation with such surface forcing compared to the idealised Campin and Goosse (1999) case, lowers the impact of the scheme). Further, in the default CG1999 case, the direct

transport of tracers downslope without a return flow leads to a change in the water mass transformation opposite to that from advection (not shown). This anti-correlation may also partly account for the result of Bates et al. (2012b) who found that, while CG1999 increased the depth of the downslope plume in an idealised test case, it decreased the downslope speed of the plume. An equivalent anti-correlation of the parameterization's downslope flow and the Eulerian advection term is found for BLOBS. The movement of Lagrangian particles replaces a portion of the Eulerian flow leading to a near zero change in tracers and density in the south. A reduction in the vertical diffusion component through applying MIXD is also observed. However, the partial convective mixing of MIXD does not counteract the vertical diffusion to the same degree as the BLOBS does to advection.

The different response of the model to MIXD and the resulting increased sensitivity of AABW and NADW indicates the partial convective mixing is the most efficient of the three processes based on CG1999 at transporting dense water down slope. This result corroborates the non-trivial impact of MIXD found the North Atlantic by Palter et al. (2014). Hence, due to the similarity of the CG1999, OVER and MIXD schemes and the minimal response produced by CG1999 and OVER for all the parameter choices given in Table 1, only results of the MIXD sensitivity analysis to changes in parameters will be presented along with SIGMA and BLOBS.

Some analysis of other regions of deep water formation was also undertaken. For example, within the Labrador Sea, the BLOBS leads to a decrease in transport of Labrador Sea Water (based on the transport within density layers at the expected Labrador Sea Water depths) out of the Labrador Sea (7% of CTR). MIXD is found to increase transport into the region (43% greater than CTR) and also decreases the transport out (59% of CTR). However, the production of Lagrangian particles and the application of MIXD within the Labrador Sea itself makes any correlation between the Nordic Sea overflows and the Labrador Sea currents and convection (Zhang et al., 2011) impossible to distinguish. Since we are interested in the overall NADW and AABW properties, further work into such deep water formation regions as the Labrador Sea is beyond the scope of this paper.

4.3. MIXD Parameter Sensitivity

We now investigate the sensitivity of AABW and NADW to MIXD with the various parameter choices given in Table 1. The greatest change caused from applying MIXD, compared to CTR, occurs when more grid cells are applied to the downslope flow (n; blue line; Figure 10) and further again when the most distant points are weighted for enhanced downslope flow (*weight*; green line; Figure 10). Both cases lead to denser (by a maximum of 0.015 kg m^{-3} compared to default MIXD and 0.027 kg m^{-3} compared to CTR) and younger (by 125 years; 15% compared to default MIXD and 525 years; 63% compared to CTR) waters penetrating deeper in the north, with minimal change occurring at the surface for each parameter variation. These results are consistent with expectations, as increasing n increases the number of instances where MIXD is activated, while *weight* enhances the transport to greatest depths.

Increasing the fraction of the grid cell participating in the overflow (δ; Equation 2.1.2) also increases the density and decreases age in the north compared to the default MIXD (also expected, as increasing δ allows a greater volume of water to participate in the overflow) but with minimal response in the south. The greatest response in the south occurs again for *weight*, increasing density and decreasing age by 0.0075 kg m^{-3} and 60 years (15%) respectively compared to default MIXD. There is little sensitivity to the salinity in the south (<10% change compared to the north), however cooler waters are produced in the south by the parameter changes.

For the change in MOC from CTR for each parameter change in MIXD (Table 1), only the *mask* case (Figure 11a) shows negligible change (<0.05 Sv) of the NADW cell from the default MIXD (Figure 9d). We remind the reader that the *mask* case only applies the MIXD scheme south of the equator. The *mask* case does, however, indicate that the NADW and AABW cell changes are uncorrelated in this case with similar change produced in the anti-clockwise AABW cell when compared to the default MIXD case. Also, there are approximately equivalent changes in the deep south region for the *mask* case and the default MIXD (Figure 10), hence the effects of each parameter change on the defined south region may be considered approximately independent of the changes in the NADW flow.

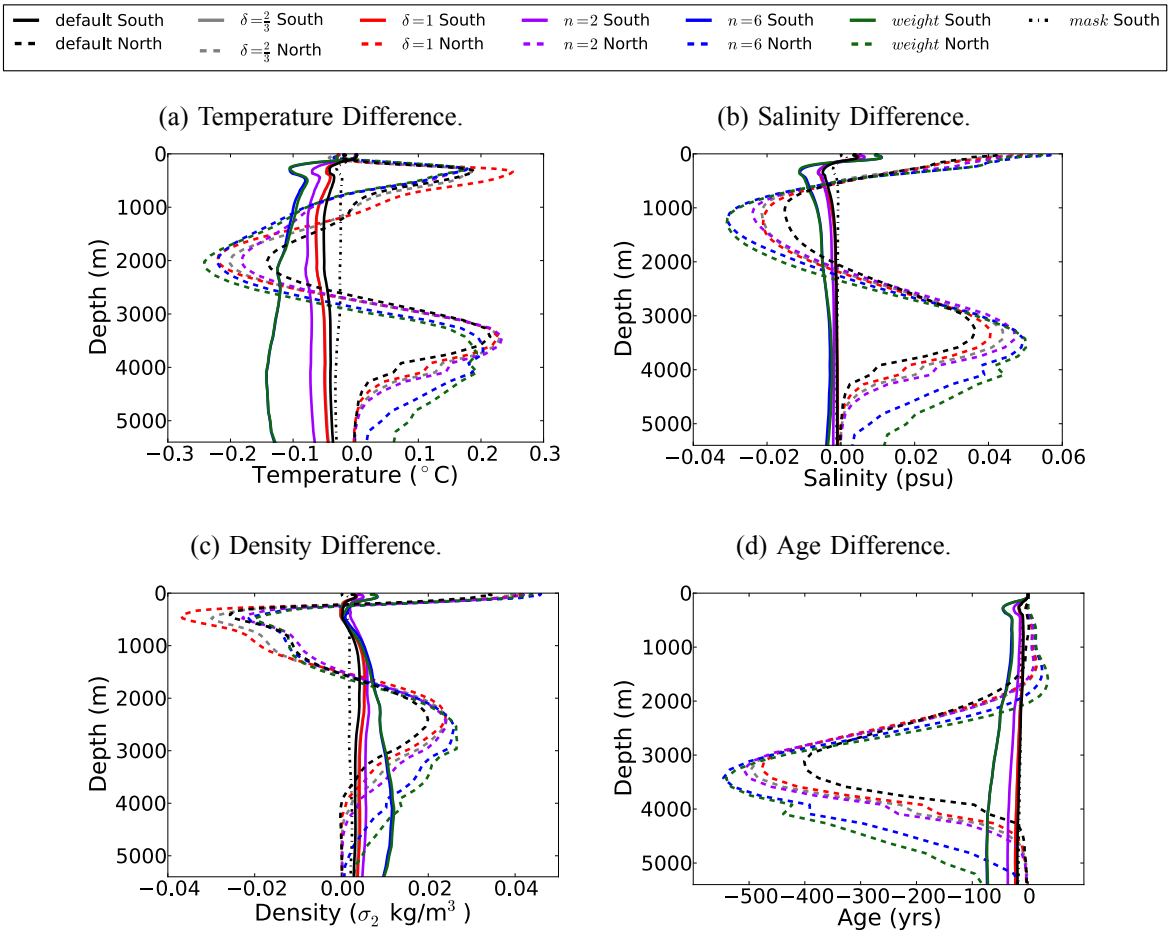

Figure 10: MIXD difference from CTR in (a) temperature (°C), (b) salinity (psu), (c) density (kg m^{-3}) and (d) age (years) averaged over the region 32.4°N-62.4°N (dashed lines) and 44.7°S-74.7°S (solid lines) versus depth for each of the different parameter changes of MIXD. The difference is defined as the time average of the last 20 years in the overflow scheme runs minus the equivalent of the CTR.

All other parameter changes lead to the NADW becoming denser at the lower edge of the clockwise cell (Figure 11) compared to the default MIXD (Figure 9d). Increasing n and applying *weight* again maximise the NADW cell MOC response and leads to a slight enhancement in the anti-clockwise AABW cell, though overall the AABW cell is less sensitive to the parameter changes.

The net transport shows an overall marginal increase in the maximum of the AABW cell at 30°S by up to 14%, while the increase in density of the NADW cells leads to an overall

Run	AABW − CTR (Sv)	NADW − CTR (Sv)
CG1999 (default)	**0.004 (↑ 0.2%)**	**-0.004 (↓ 0.1%)**
OVER (default)	**0.01 (↑ 0.5%)**	**0.01 (↑ 0.3%)**
MIXD (default)	**0.21 (↑ 10%)**	**-0.12 (↓ 3%)**
MIXD (*mask*)	0.16 (↑ 7%)	-0.01 (↓ 0.3%)
MIXD ($\delta = \frac{2}{3}$)	0.21 (↑ 10%)	-0.15 (↓ 4%)
MIXD ($\delta = 0.1$)	0.25 (↑ 11%)	-0.20 (↓ 6%)
MIXD ($n = 2$)	0.30 (↑ 14%)	-0.11 (↓ 3%)
MIXD ($n = 6$)	0.30 (↑ 14%)	-0.11 (↓ 3%)
MIXD (*weight*)	0.22 (↑ 10%)	-0.11 (↓ 3%)

Table 4: Difference from CTR of AABW and NADW transport (defined as the maximum and minimum transport for σ_2>36.6 kg m^{-3} at 30°S and 30°N respectively) for each MIXD parameter sensitivity runs as well the default CG1999 and OVER for comparison. Note the different scale of the horizontal axes to Figure 8.

decrease in the maximum NADW transport (Table 4). The transport of CG1999 and OVER is also included in Table 4 for comparison, however, due to the fundamental similarity of the schemes and the minimal change of CG1999 and OVER, we only present the comprehensive results for MIXD.

4.4. SIGMA Parameter Sensitivity

Insignificant changes (< 1%) from the default SIGMA are found in the tracer properties (Figure 12) and MOC (Figure 13a and 13b compared to Figure 9c) for variations in κ_σ^{ratio}. This lack of sensitivity to κ_σ^{ratio} indicates that an increase or decrease of the flow that does not enhance the dense downslope transport has little influence on the actual downslope transport of the dense waters. Applying a constant diffusivity is found to produce the largest change in tracers (blue line; Figure 12) and MOC (Figure 13c) compared to the default, effectively decreasing the scheme's impact (by approximately 50%) on density, age and the NADW cell. This result agrees with Tang and Roberts (2005) who investigated SIGMA in the North Atlantic and found the inclusion of an advective component (in our case the velocity dependent diffusion) increased the dense downslope flow. In contrast, Döscher and Beckmann (2000) found minimal change with the inclusion of an advective term; however, they use a diffusion coefficient of 10^4 m^2 s^{-1} in the constant diffusion case,

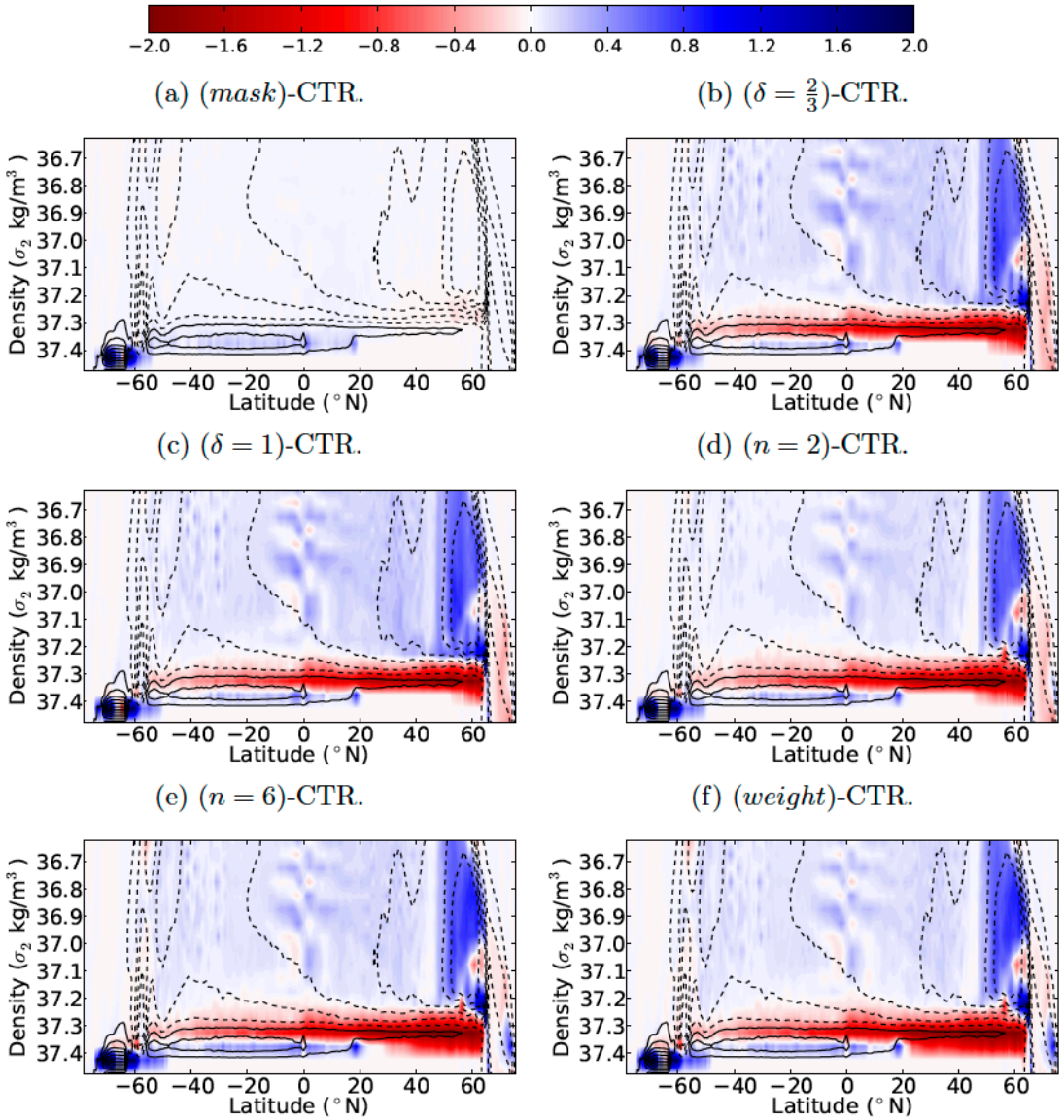

Figure 11: Difference in meridional overturning (Sv) of MIXD from the CTR in potential density space referenced to 2000 m (σ_2) for the cases (a) *mask*, (b) $\delta = \frac{2}{3}$, (c) $\delta = 1$, (d) $n = 2$, (e) $n = 6$ and (f) *weight* taken as a time mean from years 180-200 in the parameter runs. The contours represent the mean overturning of CTR in this period with solid contours indicating anti-clockwise overturning and dashed clockwise at unit intervals starting at 0.5 and -0.5 respectively.

while Tang and Roberts (2005) used 10^3 m^2 s^{-1}.

Döscher and Beckmann (2000) also indicate SIGMA produces a deepening of the upper NADW cell, increasing the depth of the MOC 0 Sv streamfunction below the NADW cell

Run	AABW − CTR (Sv)	NADW − CTR (Sv)
SIGMA (default)	**0.01 (↑ 0.5%)**	**0.02 (↑ 1%)**
SIGMA ($\kappa_\sigma^{ratio} = 10^{-4}$)	0.01 (↑ 0.5%)	0.02 (↑ 1%)
SIGMA ($\kappa_\sigma^{ratio} = 10^{-8}$)	0.01 (↑ 0.5%)	0.02 (↑ 1%)
SIGMA ($\kappa_\sigma = const$)	0.01 (↑ 0.5%)	0.01 (↑ 0.3%)

Table 5: Difference from CTR of AABW and NADW transport (defined as the maximum/minimum transport for σ_2>36.6 kg m^{-3} at 30°S and 30°N respectively) for each SIGMA parameter sensitivity runs.

from 1800 m to 2700 m. Our results do not replicate this result, again potentially due to the different diffusion coefficients, with no noticeable change (less than 50 m) in the depth of the MOC zero streamfunction compared to CTR (Figure 5b). Overall, insignificant ($\leq 1\%$) change occurs for the AABW and NADW transport (Table 5). One main disadvantage of SIGMA is that the scheme is limited to the bottom grid cells. Such a limit means dense water descending to a neutral buoyancy depth, rather than the ocean bottom, are not represented and may be reducing the scheme's overall response.

4.5. BLOBS Parameter Sensitivity

The BLOBS scheme is computationally expensive compared to the other schemes, requiring 4.8× the runtime of CTR for the default BLOBS case. The *less* case is the least computationally expensive of the BLOBS sensitivity runs (2.5× the runtime of CTR), due to the runtime dependence on the number of active Lagrangian particle (Bates, 2011). This computational expense is higher than expected (Bates, 2011), however recent code alterations (Appendix A) and the application of BLOBS in a realistic bathymetry may have influenced the runtime as well as the large number of active particles (order 10^5).

Parameter variations increasing/decreasing detrainment or entrainment produce minimal change to AABW and NADW properties and circulation (results overlap or are close to the default case of Figure 14). This low sensitivity is a consequence of the detrainment influencing the Lagrangian particles mass by only 0.0001% and entrainment by 0.1%. Due to the similarity of these results to the default BLOBS case, they are not included in the following figures and discussion.

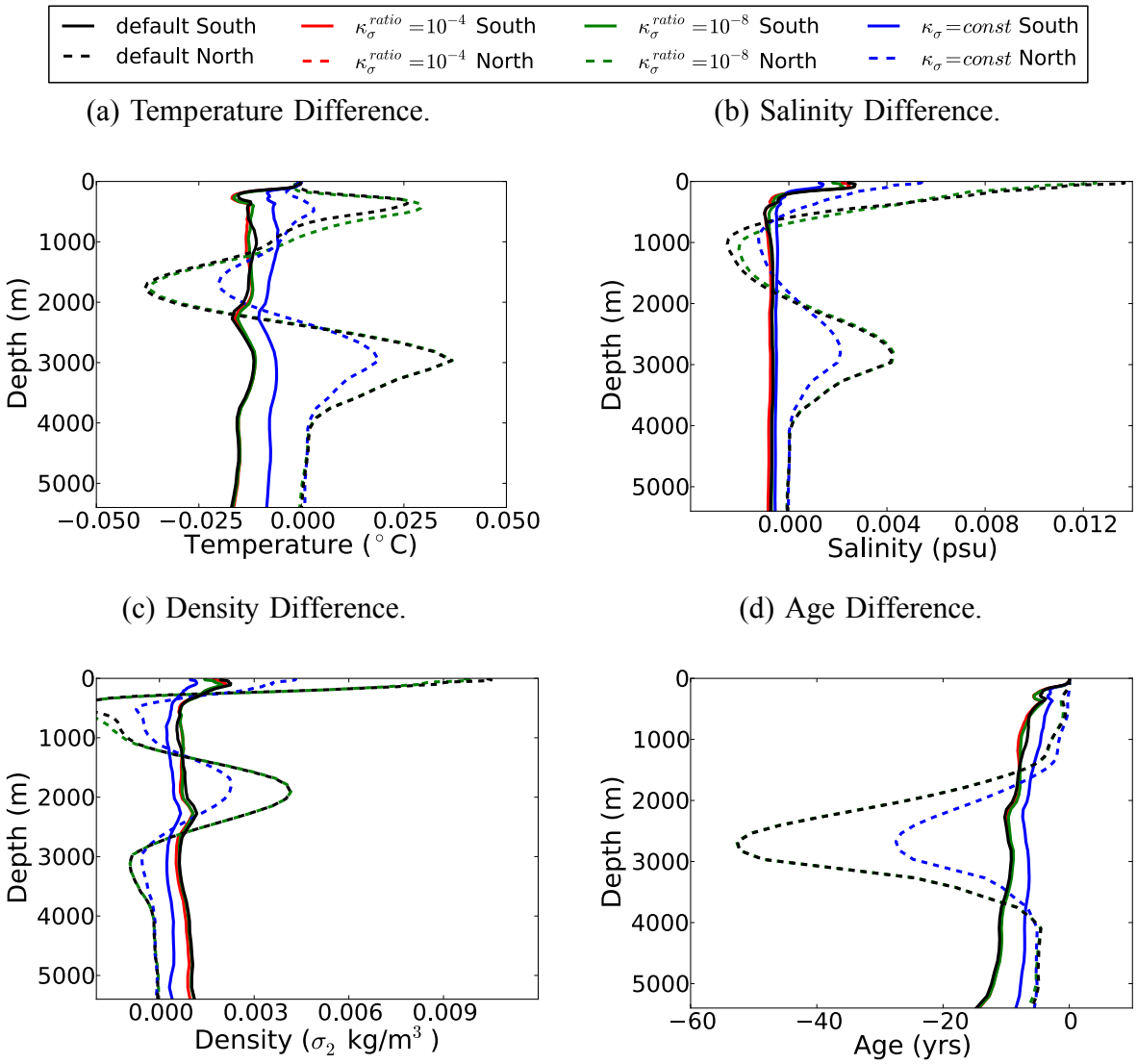

Figure 12: SIGMA difference from the CTR in (a) temperature (°C), (b) salinity (psu), (c) density (kg m^{-3}) and (d) age (years) averaged over the region 32.4°N-62.4°N (dashed lines) and 44.7°S-74.7°S (solid lines) versus depth for each of the different parameter changes of SIGMA. The difference is defined as the time average of the last 20 years in the overflow scheme runs minus the equivalent of the CTR. Note the different scale of the horizontal axes to Figure 8 and 10 in order to highlight the structure of the SIGMA scheme results.

554 AABW shows minimal sensitivity to the BLOBS scheme despite the range of parameters
555 explored. Increasing bottom drag produces the greatest change to density in the south
556 (Figure 14), increasing density by a maximum of 0.0016 kg m^{-3} compared to CTR (6% the

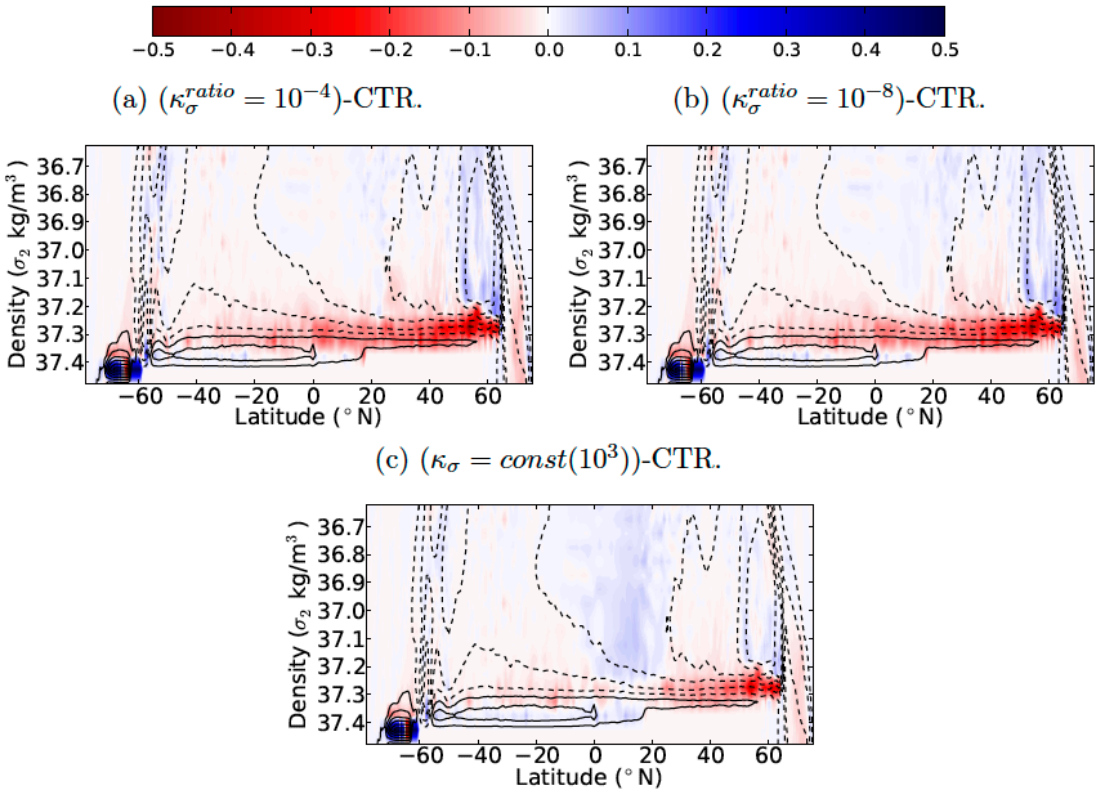

Figure 13: Difference in meridional overturning (Sv) of SIGMA from CTR in potential density space referenced to 2000 m (σ_2) for the cases (a) $\kappa_\sigma^{ratio} = 10^{-4}$, (b) $\kappa_\sigma^{ratio} = 10^{-8}$ and (c) $\kappa_\sigma = const$ taken as a time mean from years 180-200 in the parameter runs. The contours represent the mean overturning of the CTR case during the same time period with solid contours indicating anti-clockwise overturning and dashed clockwise at unit intervals starting at 0.5 and -0.5 respectively.

change produced from MIXD *weight*). Higher bottom drag acts to slow particles (Bates, 2011) and flow non-geostrophically (Bates et al., 2012b). Such non-geostrophic flow allows particles to flow directly downslope and reach deeper depths providing the greatest increase in density below 2500 m. The maximum age decrease is 24 years compared to CTR (4% the change from MIXD *weight*) and occurs for the default and $4\beta_{0b}$. All other values show negligible change in the south compared to the default BLOBS (less than 0.0003 kg m^{-3} change in density and less then 20 years (3%) change in age). Minimal change is also observed in the lower cell of the overturning circulation (Figure 15) with the largest difference in AABW strength compared to CTR being less than 1% (Table 6).

In the north, increasing bottom drag (grey in Figure 14) leads to dense water descending to greater depth, with the maximum change from CTR (0.005 kg m^{-3}) at 2200 m. Decreasing the bottom drag to $C_d = 3 \times 10^{-4}$ (red in Figure 14) increases the speed of the Lagrangian particles (Bates et al., 2012b) but does not influence the particle trajectories (they continue to flow mainly geostrophically along the slope). The faster particles lead to cooler and fresher NADW compared to the default BLOBS with little change in density. Similar results to the default BLOBS occurs when fewer particles are formed (*less* case; magenta in Figure 14). This indicates that the key overflow processes are captured when only considering steep slopes (>8 cells deep) and large density variations on the slope (>0.016 kg m^{-3}). Increasing the number of particles formed (*more* case; green in Figure 14) however increases the transport of warm salty water to depth. The combined influence of the tracers decreases the density at the maximum by 0.0006 kg m^{-3} with a decrease in age of 15 years compared to the default BLOBS.

Increasing/decreasing the Lagrangian particles size (yellow/blue lines respectively in Figure 14) increases/decreases the impact of the BLOBS scheme. The $4\beta_{0b}$ case produces for the greatest increase in density (maximum change below 1000 m of 0.0096 kg m^{-3}) and decrease in age (maximum change 115 years) in the north of all the BLOBS parameter regimes considered. Such changes are 36% the density change and 22% the age change produced by MIXD *weight* in the north.

The change from CTR in the upper cell circulation (Figure 15) shows similar characteristics for all BLOBS cases, producing an increase in the circulation of the densest portion of the cell with a decrease in the streamfunction above. The $4\beta_{0b}$ case, as with the tracer properties, imparts the greatest impact, leading to a maximum change in the upper cell of 0.7 Sv. As with MIXD however, the increase in the densest part of the NADW cell leads to a reduction in the calculated NADW maximum at 30°N (decreasing it by 1% for the $4\beta_{0b}$ case; Table 6).

While our study focusses on water mass properties, some regard of the importance of reproducing the correct overflow pathways should be considered. BLOBS is the only scheme dynamically defining the descent path of AABW and NADW. All other schemes move dense

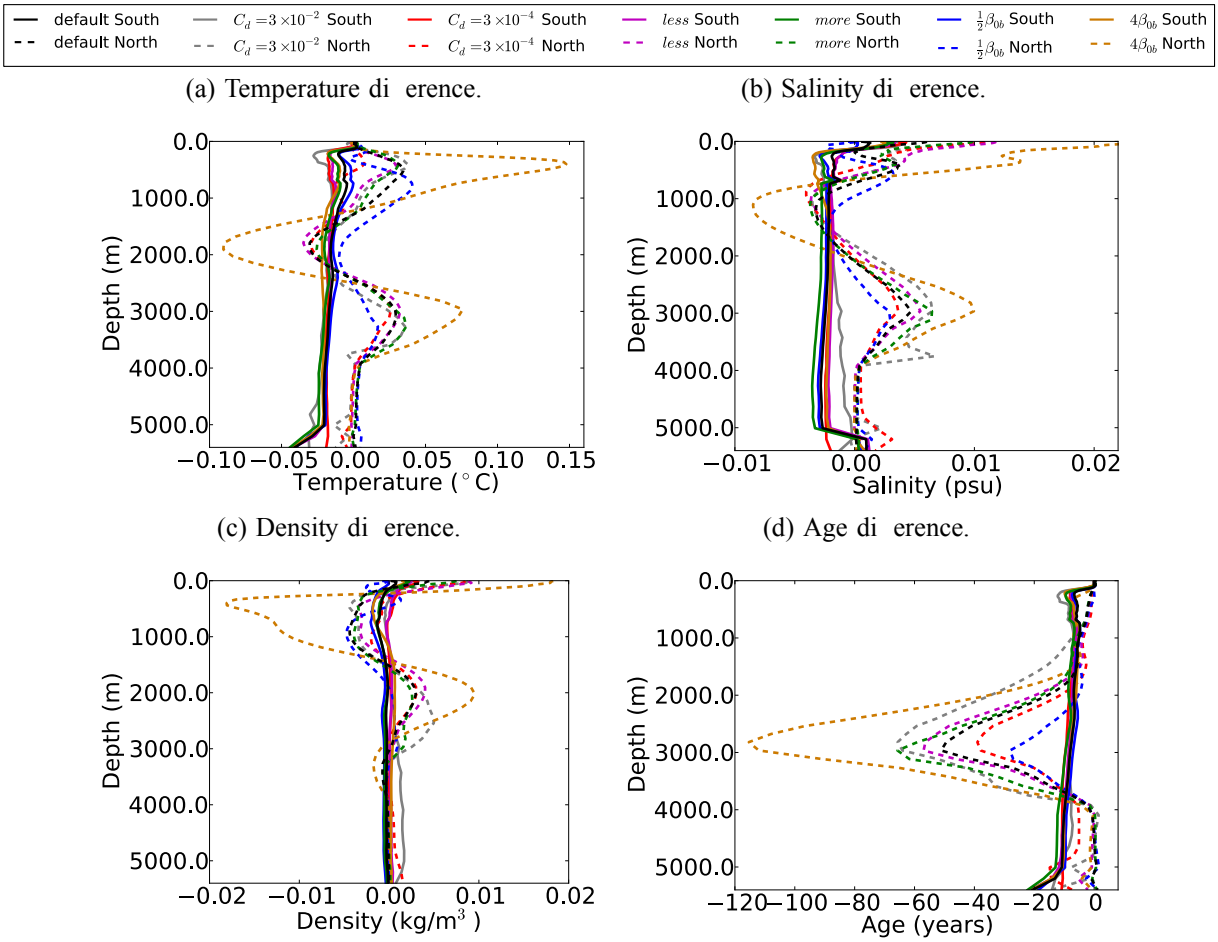

Figure 14: BLOBS difference from the CTR in (a) temperature (°C), (b) salinity (psu), (c) density (kg m^{-3}) and (d) age (years) in the region 32.4°N-62.4°N (dashed lines) and 44.7°S-74.7°S (solid lines) versus depth for each of the different parameter changes of BLOBS. The difference is defined as the time average of the last 20 years in the overflow scheme runs minus the equivalent of the CTR. Note the different scale of the horizontal axes to Figure 8, 10 and 12 in order to highlight the structure of the BLOBS scheme results.

595 water unphysically straight downslope without consideration of Coriolis forces. That is,
596 while BLOBS dynamically controls the descent of dense water, MIXD moves dense water
597 directly downslope dispersing it throughout the deep ocean. Figure 16 illustrates this point
598 where we see the change in temperature from CTR after 200 years on the bottom grid cells
599 for BLOBS and MIXD. MIXD leads to cooler water dispersed across the Weddell Sea while
600 BLOBS controls the flow of cold dense water along the overflow pathways. The way MIXD
601 disperses dense water over a large area while BLOBS confines it to its dynamical pathway,

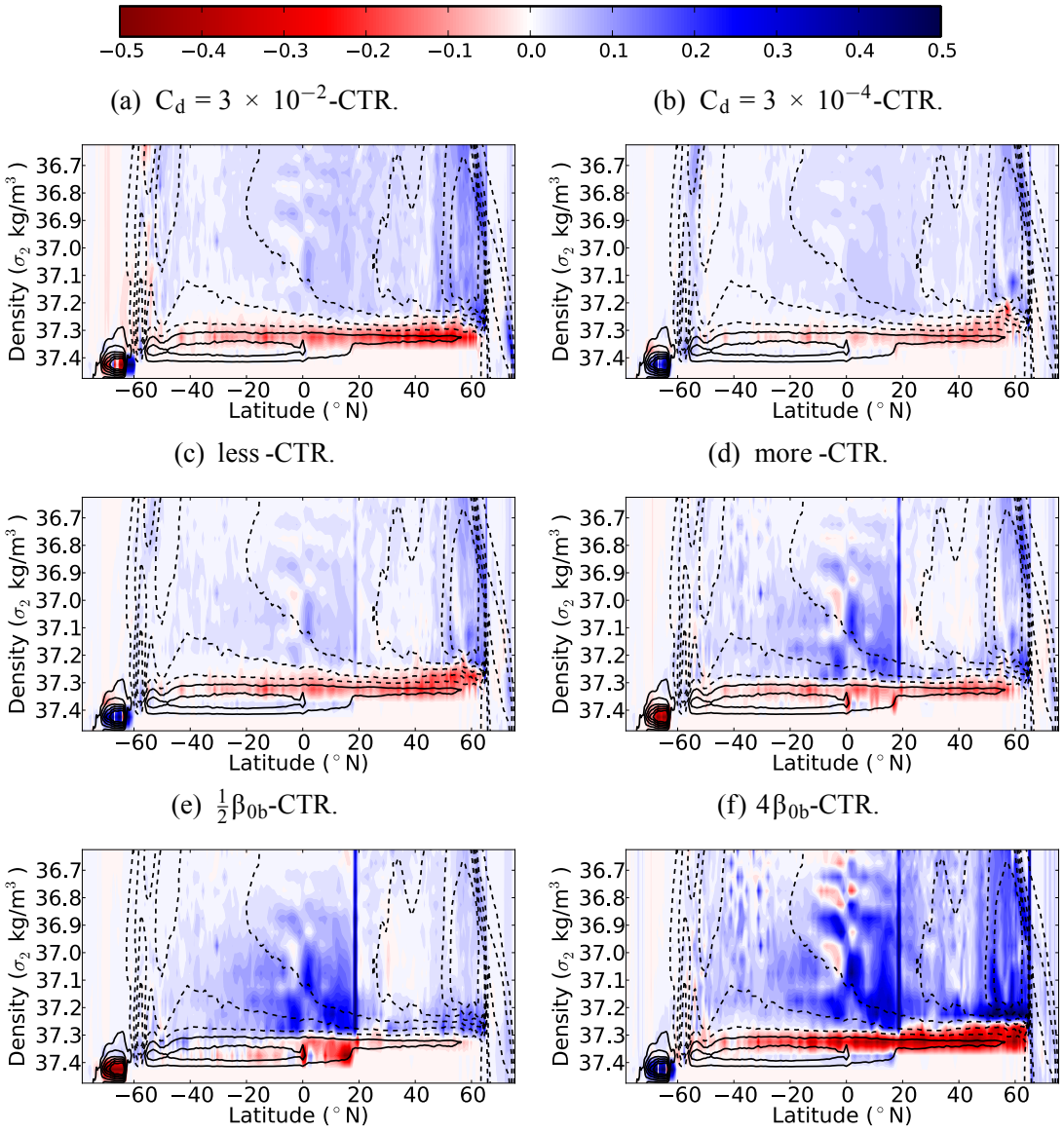

Figure 15: Difference in meridional overturning (Sv) of BLOBS from CTR in potential density space referenced to 2000 m (σ_2) for the cases (a) where $C_d = 3 \times 10^{-2}$, (b) $C_d = 3 \times 10^{-4}$, (c) *less*, (d) *more*, (e) $\frac{1}{2}\beta_{0b}$ and (f) $4\beta_{0b}$ taken as a time mean from years 180-200 in the parameter runs. The contours represent the mean overturning of the CTR case during the same time period with solid contours indicating anti-clockwise overturning and dashed clockwise at unit intervals starting at 0.5 and -0.5 respectively.

602 is likely one factor leading to MIXD producing the largest impact, while BLOBS is more
603 suitably designed for influencing deep flows within straits and passages.

Run	AABW − CTR (Sv)	NADW − CTR (Sv)
BLOBS (default)	0.017 (↑ 0.8%)	-0.024 (↓ 0.7%)
BLOBS ($4\beta_{0b}$)	0.014 (↑ 0.6%)	-0.04 (↓ 1.1%)
BLOBS ($0.5\beta_{0b}$)	-0.006 (↓ 0.3%)	-0.03 (↓ 0.9%)
BLOBS ($C_d = 3 \times 10^{-2}$)	-0.027 (↓ 1.2%)	-0.017 (↓ 0.5%)
BLOBS ($C_d = 3 \times 10^{-4}$)	0.011 (↑ 0.5%)	-0.012 (↓ 0.3%)
BLOBS (*more*)	0.003 (↑ 0.1%)	-0.005 (↓ 0.1%)
BLOBS (*less*)	0.017 (↑ 0.8%)	-0.0004 (↓ 0.0%)

Table 6: Difference from CTR of AABW and NADW transport (defined as the maximum/minimum transport for σ_2>36.6 kg m^{-3} at 30°S and 30°N respectively) for each BLOBS parameter sensitivity runs.

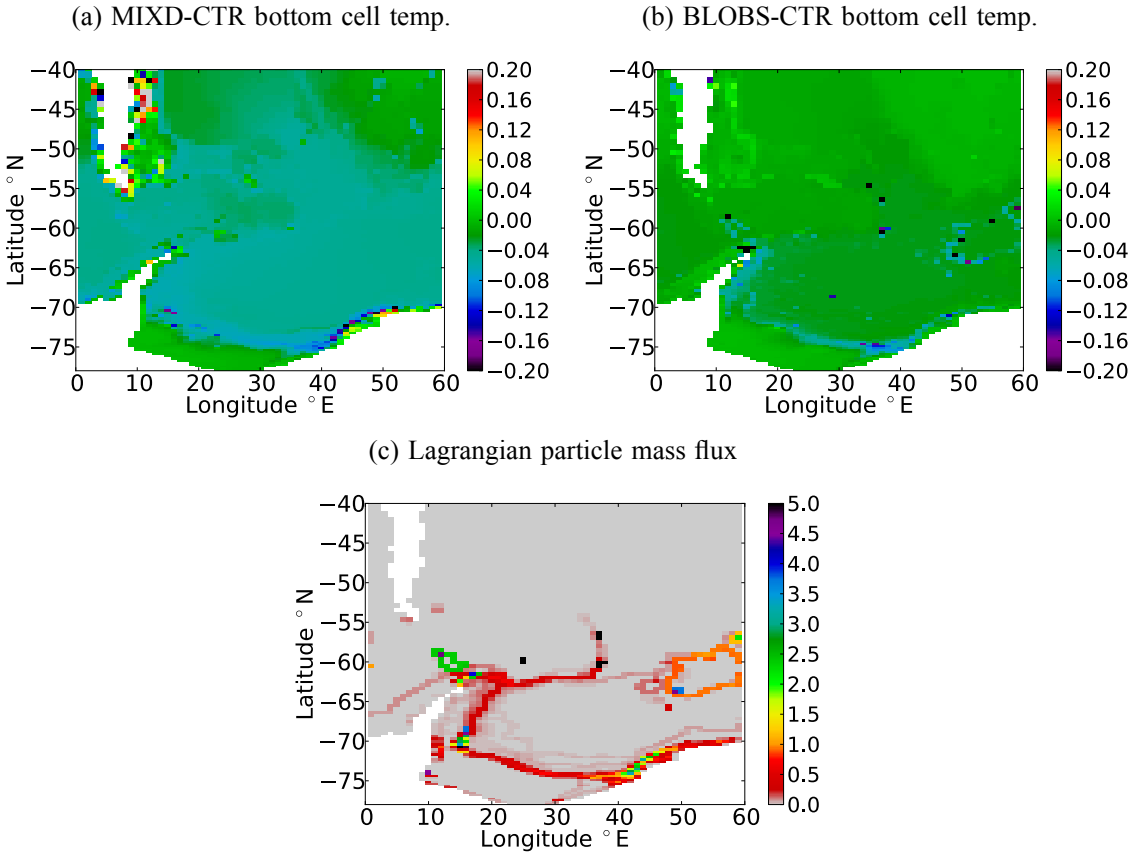

Figure 16: Difference from CTR in bottom grid cell temperature (°C) at year 200 for (a) default MIXD and (b) default BLOBS case with (c) the Lagrangian particle mass flux (1×10^{14} kg/s) entering a grid cell for the default BLOBS case over year 200. Note that we only show the mass flux into the grid cell not also the mass flux out of a grid cell. This is done in order to make the Lagrangian particle paths clearer.

5. Conclusions

Many commonly used ocean climate models struggle to represent or parameterize the observed AABW and NADW deep water properties. The application of overflow parameterizations seeks to improve the representation of these water masses. Many parameterizations are successful at improving northern dense water flow, however those tested here are unable to provide an equivalent sensitivity in the south.

MIXD (and in turn CG1999, OVER) and SIGMA overflow schemes only consider the tracer equation in their adjustment. The fully dynamical scheme of BLOBS on the other hand was designed to provide a more complete representation of overflow processes. The large NADW response provided by MIXD indicates that adjustment through dynamical factors such as the effects of the momentum of the water parcel, are not necessary for the overflow parameterization to enhance northern downslope flow. The computational cost of BLOBS compared to MIXD further makes BLOBS unviable for current GCM application, while MIXD is already suitably implemented in some GCMs. However, while our study assessed the sensitivity of AABW and NADW water mass properties, some consideration of overflow pathways may be important, with accurate pathways only represented through the dynamical BLOBS scheme.

The maximum response in the south (via the *weight* MIXD set-up) shows the comparable sensitivity of AABW to NADW is always less than 1/3 when considering the vertically integrated tracer and density changes. The reduced response from any parameterization in the south implies that the characteristics of AABW overflows cannot be substantially improved through the application of the existing overflow parameterizations investigated here. This lack of sensitivity may result from the differing characteristics of the AABW overflows. AABW overflows are more dispersed than NADW overflows and are likely less well resolved across the shelf and slope. The dispersed nature of AABW also makes alternative schemes not tested here, such as the POP overflow parameterization (Danabasoglu et al., 2010) potentially difficult to implement for AABW. Alternative approaches need to be considered (e.g. investigation into the shelf water properties or implementation of a dynamical pip-

ing scheme in BLOBS that reduces its influence on the Eulerian model), if progress into improving AABW properties in z-coordinate GCMs is to be achieved.

Acknowledgements

We thank Marshall Ward for his ongoing technical assistance and infinite availability for questions during the initial set-up of the model.This work was undertaken using the National Facility of the National Computational Infrastructure at the ANU. BMS was supported by the Australian Government Department of the Environment, and CSIRO through the Australian Climate Change Science Programme. AMH was supported by an Australian Research Council Future Fellowship FT120100842. Finally, we thank the anonymous reviewers for their efforts and thoughtful comments.

Appendix A. BLOBS code in MOM5 distribution

A slight omission in the code of the MOM5 distribution was discovered during recent testing of the BLOBS. This error meant that ocean sea surface height (SSH) contributions from the Lagrangian particle mass was not taken into account during the fast barotropic time step of the ocean model and led to abnormally large SSH (up to ± 30 m). These large SSH anomalies occurred in concentrated Largrangian particle formation regions on the shelf and produced a strong barotropic flow off the shelf. Such flow off the shelf led to an unphysical increase in dense water transport and circulation. Updating the MOM5 code to include the Lagrangian particles within the barotropic time step led to no significant change in the presented dye concentration results of the DOME test case of Bates et al. (2012b) since these results were presented after only 28 days of simulation. For the BOWL test case, however, results after one year proved long enough for the SSH anomaly to build and significantly alter the magnitude of the presented barotropic quasi-streamfunction. The updated streamfunction and bottom temperature results for the BLOBS "ctrl" case of (Bates et al., 2012b) (Figure A.17) shows an overall increase in the quasi-barotropic streamfunction, however of order 220 Sv rather than 1200 Sv. This streamfunction illustrates a greater

increase in circulation compared to all other overflow parameterizations cases of (Bates et al., 2012b) except the no return flow (Campin and Goosse, 1999) case which produces a barotropic quasi-streamfunction of order 250 Sv.

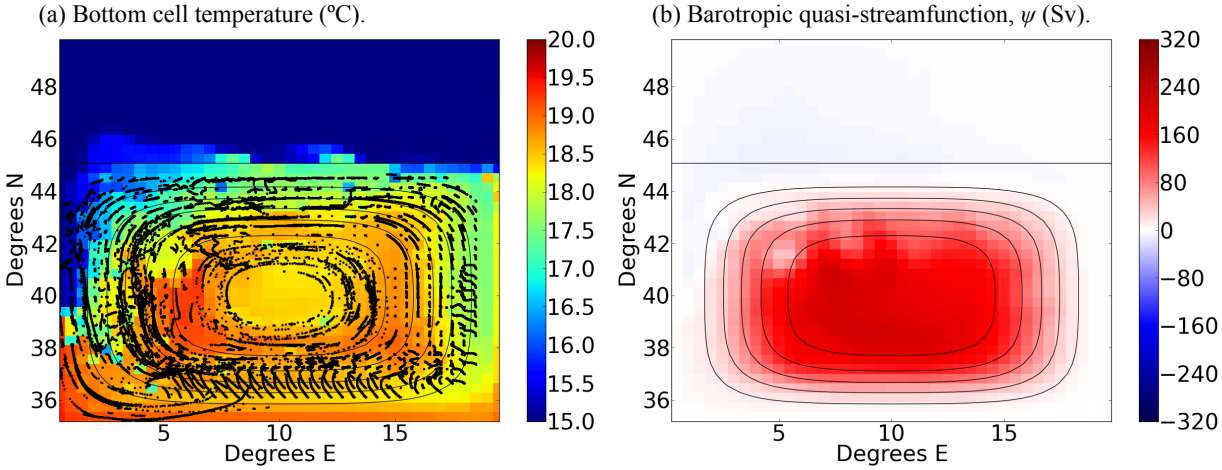

Figure A.17: (a) Bottom cell temperature (°C) and (b) barotropic quasi-streamfunction (Sv) of the "ctrl" bowl case of (Bates et al., 2012b) after one year, applying the updated MOM5 code. The black dots of (a) show the locations of the Lagrangian particles over the one year simulation.

Appendix B. Frazil Ice Parameterization

Both linear and non-linear equations may be used to define to frazil ice formation in MOM5. The linear equation computes the freezing temperature of sea water (T_f) as a linear function of salinity (S);

$$T_f = a_1 S, \tag{B.1}$$

where a_1 is a constant (Griffies, 2012). The non-linear form instead determines T_f as a nonlinear function of salinity and gauge pressure (p);

$$T_f = \frac{a_0 + S(a_1 + \sqrt{S}(a_2 + \sqrt{S}a_3)) + p(a_4 + p(a_5 + Sa_6)}{b_0 + p(b_1 + pb_2) + S^{\frac{5}{2}}b_3}, \tag{B.2}$$

where a_0, a_1, a_2, a_3, a_4, a_5, a_6, b_0, b_1, b_2 and b_3 are constants (Jackett et al., 2006). To test the two forms of T_f, the model and set-up defined in Section 3.1 and 3.2 was used at $\frac{1}{4}^\circ$ resolution and without the application of the Gent and McWilliams (1990) eddy parameterization. The model is run for 280 yrs with the non-linear equation defining frazil formation applied. Two runs are then performed for 15 yrs, one with the linear form (Equation B.1) and the other continuing the non-linear form (Equation B.2). After 15 yrs, the non-linear forms leads to a significant increase in ice mass compared to the linear case (Figure B.18d) and is most pronounced in the southern hemisphere. The non-linear form also produces cooler and saltier waters on the southern shelf, resulting in an overall increase in density on the Antarctic shelf by up to 0.05 kg m^{-3} (Figure B.18).

References

Baines PG, Condie S. Observations and modelling of Antarctic downslope flows: A review. Ocean, Ice, and Atmosphere: Interactions at the Antarctic Continental Margin 1998;75.

Bates ML. A dynamic, embedded Lagrangian model for ocean climate models. Ph.D. thesis; University of New South Wales; 2011.

Bates ML, Griffies SM, England MH. A dynamic, embedded Lagrangian model for ocean climate models. Part I: Theory and implementation. Ocean Modelling 2012a;59-60.

Bates ML, Griffies SM, England MH. A dynamic, embedded Lagrangian model for ocean climate models, Part II: Idealised overflow tests. Ocean Modelling 2012b;59-60.

Beckmann A, Döscher R. A method for improved representation of dense water spreading over topography in geopotential-coordinate models. Journal of Physical Oceanography 1997;27:581–91.

Bi D, Marsland SJ, Uotila P, O'Farrell S, Fiedler R, Sullivan A, Griffies S, Zhou X, Hirst A. ACCESS-OM: the ocean and sea ice core of the ACCESS coupled model. Australian Meteorological and Oceanographic Journal 2013;63:213–32.

Campin JM, Goosse H. Parameterization of density-driven downsloping flow for a coarse-resolution ocean model in z-coordinates. Tellus 1999;51A:412–30.

Chan W, Motoi T. Effects of stopping the Mediterranean outflow on the southern polar region. Polar Meteorology and Glaciology 2003;17:25–35.

Condie SA. Descent of dense water masses along continental slopes. Journal of Marine Research 1995;53:897–928.

Couldrey MP, Jullion L, Garabato ACN, Rye C, Herráiz-Borreguero L, Brown PJ, Meredith MP, Speer

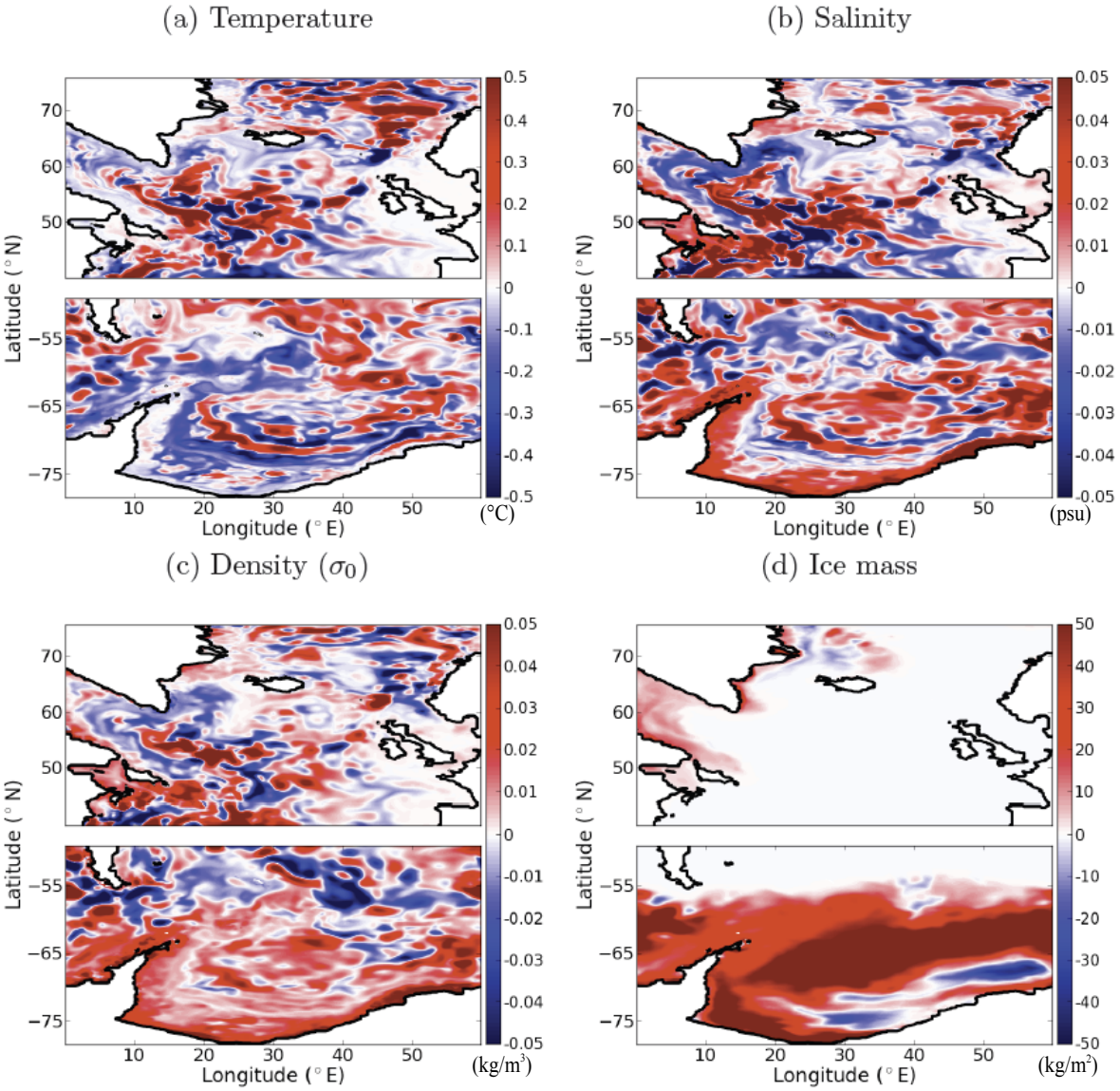

Figure B.18: Yearly mean difference in applying a non-linear to linear equation for defining the freezing temperature of seawater for frazil formation for (a) temperature (°C), (b) salinity (psu), (c) potential density referenced to 0 m (σ_0; kg m^{-3}) and (d) ice mass (kg m^{-2}). Temperature, salinity and density are depth averaged on the shelf for values above 1300 m.

KL. Remotely induced warming of Antarctic Bottom Water in the eastern Weddell gyre. Geophysical Research Letters 2013;40:2755–60.

Danabasoglu G, Large W, Briegleb B. Climate impacts of parameterized Nordic Sea overflows. Journal of Geophysical Research 2010;115, C11005. doi:10.1029/2010JC006243.

Danabasoglu G, Yeager SG, Bailey D, Behrens E, Bentsen M, Bi D, Biastoch A, Böning C, Bozec A, Canuto VM, Cassou C, Chassignet E, Coward AC, Danilov S, Diansky N, Drange H, Farneti R, Fernandez E, Fogli PG, Forget G, Fujii Y, Griffies SM, Gusev A, Heimbach P, Howard A, Jung T, Kelley M, Large WG, Leboissetier A, Lu J, Madec G, Marsland SJ, Masina S, Navarra A, Nurser AG, Pirani A, y Mélia DS, Samuels BL, Scheinert M, Sidorenko D, Treguier A, Tsujino H, Uotila P, Valcke S, Voldoire A, Wangi Q. North Atlantic simulations in Coordinated Ocean-ice Reference Experiments phase II (CORE-II). Part I: Mean states. Ocean Modelling 2014;73:76–107.

Deacon GER. The hydrology of the Southern Ocean. volume 15 of *Discovery reports*. Cambridge University Press, 1937.

Delworth TL, Rosati A, Anderson W, Adcroft AJ, Balaji V, Benson R, Dixon K, Griffies SM, Lee HC, Pacanowski RC, Vecchi GA, Wittenberg AT, Zeng F, Zhang R. Simulated climate and climate change in the GFDL CM2.5 high-resolution coupled climate model. Journal of Climate 2012;25:2755–81.

Döscher R, Beckmann A. Effects of a bottom boundary layer parameterisation in a coarse-resolution model of the North Atlantic Ocean. Journal of Atmospheric and Oceanic Technology 2000;17:698–707.

Downes SM, Gnanadesikan A, Griffies SM, Sarmiento JL. Water mass exchange in the Southern Ocean in coupling climate models. Journal of Physical Oceanography 2011;41:1756–71.

Dunne JP, John JG, Hallberg RW, Griffies SM, Shevliakova EN, Stouffer RJ, Krasting JP, Sentman LA, Milly PCD, Malyshev SL, Adcroft AJ, Cooke W, Dunne KA, Harrison MJ, Levy H, Samuels BL, Spelman M, Winton M, Wittenberg AT, Phillips PJ, Zadeh N. GFDLs ESM2 global coupled climate-carbon Earth System Models Part I: Physical formulation and baseline simulation characteristics. Journal of Climate 2012;25:6646–6665.

Ezer T, Mellor GL. Diagnostic and prognostic calculations of the North Atlantic circulation and sea level using sigma co-ordinate ocean model. Journal of Geophysical Research 1994;99:14159–71.

Ezer T, Mellor GL. A generalized coordinate ocean model and a comparison of the bottom boundary layer dynamics in terrain-following and in z-level grids. Ocean Modelling 2004;6:379–403.

Foldvik A, Gammelsrød T, Østerhus S, Fahrbach E, Rohardt G, Schröder M, Nicholls KW, Padman L, Woodgate RA. Ice shelf water overflow and bottom water formation in the southern Weddell Sea. Journal of Geophysical Research 2004;109. doi:10.1029/2003JC002008.

Fox-Kemper B, Ferrari R, Hallberg RW. Parameterization of mixed layer eddies. Part I: Theory and diagnosis. Journal of Physical Oceanography 2008;38:1145–65.

Frajka-Williams E, Cunningham SA, Bryden H, King BA. Variability of Antarctic Bottom Water at 24.5°N in the Atlantic. Journal of Geophysical Research 2011;116(C11026). doi:10.1029/2011JC007168.

Garcia H, Cruzado A, Gordon L, Escanez J. Decadal-scale chemical variability in the subtropical North Atlantic deduced from nutrient and oxygen data. Journal of Geophysical Research 1998;103:2817–30.

Gent P, McWilliams JC. Isopycnal mixing in ocean circulation models. Journal of Physical Oceanography 1990;20:150–5.

Gerdes R, Hurlin WJ, Griffies SM. Sensitivity of a global ocean model to increased run-off from Greenland. Ocean Modelling 2006;12:416–35.

Goosse H, Campin JM, Tartinville B. The sources of Antarctic bottom water in a global ice-ocean model. Ocean Modelling 2001;3:51–65.

Gordon AL, Huber BA, Hellmer HH, Ffield A. Deep and bottom water of the Weddell Seas western rim. Science 1993;262:95–7.

Griffies SM. Elements of the Modular Ocean Model (MOM). GFDL Ocean Group Technical Report No. 7. NOAA/Geophysical Fluid Dynamics Laboratory, 2012. Http://www.mom-ocean.org/web/docs.

Griffies SM, Böning C, Bryan FO, Chassignet EP, Gerdes R, Hasumi H, Hirst A, Treguier A, Webb D. Developments in ocean climate modelling. Ocean Modelling 2000;2:123–92.

Griffies SM, Hallberg RW. Biharmonic friction with a Smagorinsky viscosity for use in large-scale eddy-permitting ocean models. Monthly Weather Review 2000;128:2935–46.

Hall MM, McCartney M, Whitehead JA. Antarctic Bottom Water flux in the equatorial Western Atlantic. Journal of Physical Oceanography 1997;27:1903–26.

Heuzé C, Heywood KJ, Stevens DP, Ridley JK. Southern Ocean bottom water characteristics in CMIP5 models. Geophysical Research Letters 2013;40:1409–14.

Hogg AM, Dijkstra HA, Saenz JA. The energetics of a collapsing meridional overturning circulation. Journal of Physical Oceanography 2013;43:1512–24.

Hughes GO, Griffiths RW. A simple convective model of the global overturning circulation, including effects of entrainment into sinking regions. Ocean Modelling 2006;12:46–79.

Ivanovic RF, Valdes PJ, Gregoire L, Flecker R, Gutjahr M. Sensitivity of modern climate to the presence, strength and salinity of Mediterranean-Atlantic exchange in a global general circulation model. Climate Dynamics 2014;42:859–77.

Jackett DR, McDougall TJ, Feistel R, Wright DG, Griffies SM. Algorithms for density, potential temperature, conservative temperature, and freezing temperature of seawater. Journal of Atmospheric and Oceanic Technology 2006;23:1709–28.

Johns WE, Baringer MO, Beal LM, Cunningham SA, Kanzow T, Bryden HL, Hitschi JJM, Marotzke J, Meinen CS, Shaw B, Curry R. Continuous, array-based estimates of Atlantic Ocean heat transport at 26.5°N. Journal of Climate 2011;24:2429–49.

Johnson GC. Quantifying Antarctic Bottom Water and North Atlantic Deep Water volumes. Journal of Geophysical Research 2008;113(C05027). doi:10.1029/2007JC004477.

Katsumata K, Masuda S. Variability in southern hemisphere ocean circulation from the 1980s to the 2000s.

770 Journal of Physical Oceanography 2013;43:1981–2007.

771 Kuhlbrodt T, Griesel A, Montoya M, Levermann A, Hofmann M, Rahmstorf S. On the driving pro-
772 cesses of the Atlantic meridional overturning circulation. Reviews of Geophysics 2007;45(RG2001).
773 doi:10.1029/2004RG000166.

774 Large WG, McWilliams JC, Doney SC. Oceanic vertical mixing: A review and a model with a nonlocal
775 boundary layer parameterization. Reviews in Geophysics 1994;32:363–403.

776 Large WG, Yeager S. The global climatology of an interannually varying air-sea flux data sets. Climate
777 Dynamics; 2009. doi:10.1007/s00382-008-0441-3.

778 Lee HC, Rosati A, Spelman MJ. Barotropic tidal mixing effects in a coupled climate model: oceanic
779 conditions in the Northern Atlantic. Ocean Modelling 2006;11:464–77.

780 Legg S, Briegleb B, Chang Y, Chassignet EP, Danabasoglu G, Ezer T, Gordon AL, Griffies S, Hallberg
781 R, Jackson L, Large W, Özgökmen TM, Peters H, Price J, Riemenschneider U, Wu W, Xu X, Yang J.
782 Improving oceanic overflow representation in climate models: The gravity current entrainment climate
783 process team. Bulletin of the American Meteorological Society 2009;90:657–70.

784 Legg S, Hallberg RW, Girton JB. Comparison of entrainment in overflows simulated by z-coordinate,
785 isopycnal and non-hydrostatic models. Ocean Modelling 2006;11:69–97.

786 Levitus S, Antonov J, Boyer T. Warming of the world ocean, 19552003. Geophysical Research Letters
787 2005;32(L02604). doi:10.1029/2004GL021592.

788 Marsland SJ, Bi D, Uotila P, Fiedler R, Griffies SM, Lorbacher K, O'Farrell S, Sullivan A, Uhe P, Zhou
789 X, Hirst AC. Evaluation of ACCESS climate model ocean metrics in CMIP5 simulations. Australian
790 Meteorological and Oceanographic Journal 2013;63:101–19.

791 McDougall TJ. Thermobaricity and cabbeling and water-mass conversion. Journal of Geophysical Research
792 1987;92(C5):5448–64.

793 Meredith MP, Woodworth PL, Chereskin TK, Marshall DP, Allison LC, Bigg GR, Donohue K, Hey-
794 wood KJ, Hughes CW, Hibbert A, Hogg AM, Johnson HL, Jullion L, King BA, Leach H, Lenn Y,
795 Morales Maqueda MA, Munday DR, Sallée ACNCPJB, Sprintall J. Sustained monitoring of the South-
796 ern Ocean at Drake Passage: Past achievements and future priorities. Reviews of Geophysics 2011;49.
797 doi:10.1029/2010RG000348.

798 Munday DR, Johnson HL, Marshall DP. Eddy saturation of equilibrated circumpolar currents. Journal of
799 Physical Oceanography 2013;43:507–32.

800 Naveira Garabato AC, McDonagh EL, Stevens DP, Heywood KJ, Sanders RJ. On the export of Antarctic
801 Bottom Water from the Weddell Sea. Deep-Sea Research II 2002;49:4715–42.

802 Orsi AH, Johnson GC, Bullister JL. Circulation, mixing and production of Antarctic Bottom Water.
803 Progress in Oceanography 1999;43:55–109.

804 Palter JB, Griffies SM, Galbraith ED, Gnanadesikan A, Samuels BL, Klocker A. The deep
805 ocean buoyancy budget and its temporal variability. Journal of Climate 2014;27:551–73.
806 doi:http://dx.doi.org/10.1175/JCLI-D-13-00016.1.
807 Price JF, Baringer MO. Outflows and deep water production by marginal seas. Progress in Oceanography
808 1994;33:161–200.
809 Purkey SG, Johnson GC. Warming of global abyssal and deep Southern Ocean waters between the 1990s
810 and 2000s: Contributions to global heat and sea level rise budgets. Journal of Climate 2010;23:6336–51.
811 Purkey SG, Johnson GC. Global contraction of Antarctic Bottom Water between the 1980s and 2000s.
812 Journal of Climate 2012;25:5830–44.
813 Rahmstorf S. On the freshwater forcing and transport of the Atlantic thermohaline circulation. Climate
814 Dynamics 1998;12:799–811.
815 Ríos AF, Velo A, Pardo PC, Hoppema M, Pérez FF. An update of anthropogenic CO_2 storage rates in
816 the western South Atlantic basin and the role of Antarctic Bottom Water. Journal of Marine Systems
817 2012;94:197–203.
818 Roberts MJ, Wood RA. Topographic sensitivity studies with a Bryan-Cox-type ocean model. Journal of
819 Physical Oceanography 1997;274:823–36.
820 van Sebille E, Spence P, Mazloff MR, England MH, Rintoul SR, Saenko OA. Abyssal connections of Antarctic
821 Bottom Water in a Southern Ocean State Estimate. Journal of Physical Oceanography 2013;28:2163–74.
822 Simmons L, Jayne SR, Laurnet LCS, Weaver AJ. Tidally driven mixing in a numerical model of the ocean
823 general circulation. Ocean Modelling 2004;6:245–63.
824 Sloyan BM, Wijffels SE, Tilbrook B, Katsumata K, Murata A, Macdonald AM. Deep ocean changes near
825 the western boundary of the South Pacific Ocean. Journal of Physical Oceanography 2013;43:2132–41.
826 Sprintall J, Wijffels SE, Molcard R, Jaya I. Direct estimates of the Indonesian Throughflow entering the
827 Indian Osean. Journal of Geophysical Research 2009;114(C07001). doi:10.1029/2008JC005257.
828 Steinfeldt R, Rhein M, Walter M. NADW transformation at the western boundary between 66 degrees
829 W/20 degrees N and 60 degrees W/10 degrees N. Deep Sea Research Part I 2007;54:835–55.
830 Talley LD, Reid JL, Robbins PE. Data-based meridional overturning streamfunctions for the global ocean.
831 Journal of Climate 2003;16:3213–26.
832 Tang YM, Roberts MJ. The impact of a bottom boundary layer scheme on the North Atlantic Ocean in a
833 global coupled climate model. Journal of Physical Oceanography 2005;35:202–17.
834 Urakawa LS, Hasumi H. Eddy-resolving model estimate of the cabbeling effect on the water mass transfor-
835 mation in the Southern Ocean. Journal of Physical Oceanography 2012;42:1288–302.
836 U.S. Department of Commerce, National Oceanic and Atmospheric Administration, Na-
837 tional Geophysical Data Center . 2-minute gridded global relief data (ETOPO2). 2001.

838 [http://www.ngdc.noaa.gov/mgg/fliers/01mgg04.html].
839 Weijer W, Sloyan BM, Maltrud ME, Jeffery N, Hecht MW, Hartin CA, Sebille EV, Wainer I, Landrum L.
840 The Southern Ocean and its climate in CCSM4. Journal of Climate 2012;25:2652–75.
841 Winton M. A reformulated three-layer sea ice model. Journal of Atmospheric and Oceanic Technology
842 2000;17:525–31.
843 Winton M, Hallberg R, Gnanadesikan A. Simulation of density-driven frictional downslope flow in z-
844 coordinate ocean models. Geophysical Research Letters 1998;40:2177–82.
845 Zenk W, Visbeck M. Structure and evolution of the abyssal jet in the Vema Channel of the South Atlantic.
846 Deep Sea Research II 2013;85:244–60.
847 Zhang R, Delworth TL, Rosati A, Anderson WG, Dixon KW, Lee HC, Zeng F. Sensitivity of the North
848 Atlantic ocean circulation to an abrupt change in the Nordic Sea overflow in a high resolution global
849 coupled climate model. Journal of Geophysical Research 2011;116(C12024). doi:10.1029/2010GL044474.